frontiers | Frontiers in Nanotechnology

TYPE Original Research
PUBLISHED 29 March 2023
DOI 10.3389/fnano.2023.1132783

OPEN ACCESS

EDITED BY
Gerson Nakazato,
State University of Londrina, Brazil

REVIEWED BY
Puneet Khandelwal,
Johns Hopkins Medicine, United States
Pramod K. Gupta,
Fraunhofer USA (FHG), United States
Hongwu Sun,
Third Military Medical University, China
Sri Ramulu Torati,
Old Dominion University, United States
Ateet Dutt,
National Autonomous University of Mexico, Mexico

*CORRESPONDENCE
Duraipandian Thavaselvam,
dtselvam.drde@gov.in

SPECIALTY SECTION
This article was submitted to Biomedical Nanotechnology, a section of the journal Frontiers in Nanotechnology

RECEIVED 27 December 2022
ACCEPTED 20 February 2023
PUBLISHED 29 March 2023

CITATION
Hans R, Yadav PK, Zaman MB, Poolla R and Thavaselvam D (2023), A rapid direct-differential agglutination assay for *Brucella* detection using antibodies conjugated with functionalized gold nanoparticles.
Front. Nanotechnol. 5:1132783.
doi: 10.3389/fnano.2023.1132783

A rapid direct-differential agglutination assay for *Brucella* detection using antibodies conjugated with functionalized gold nanoparticles

Richa Hans[1], Pranjal Kumar Yadav[1], M. Burhanuz Zaman[2], Rajaram Poolla[2] and Duraipandian Thavaselvam[3]*

[1]Division of Biodetector Development Test and Evaluation, Defence Research and Development Establishment (DRDO), Gwalior, Madhya Pradesh, India, [2]School of Studies in Physics, Jiwaji University, Gwalior, Madhya Pradesh, India, [3]Director General Life Sciences (DGLS) Office, Defence Research and Development Organization (DRDO) Headquarters, Ministry of Defence, SSPL Campus, Timarpur, New Delhi, India

Brucellosis is the most widespread and serious zoonotic disease worldwide which affects livestock, sylvatic wildlife, marine dwellers, and humans. It is acquired through Alphaproteobacteria which belong to the genus *Brucella* and is categorized as a potential bio-threat agent. In this study, we developed a rapid and direct differential whole cell (WC) agglutination-based assay for its on-field detection. The recombinant outer membrane (rOmp28) protein-derived specific mice IgG polyclonal antibodies (pAbs) of *Brucella* were purified using affinity chromatography and conjugated with functionalized gold nanoparticles (AuNPs) for rapid agglutination. A positive blot of 32 kDa protein revealed specific immuno-reactivity of rOmp28-pAbs using immunoblot analysis. For the synthesis of AuNPs, the conventional "Turkevich method" was optimized at a concentration < 1 mM of gold precursor for obtaining 50-nm-sized particles. Also, their physico-chemical characteristics were analyzed using UV-visible spectrophotometry, Fourier transform infra-red spectroscopy (FT-IR), Raman spectroscopy, X-ray diffraction (XRD), scanning electron microscopy (SEM), transmission electron microscopy (TEM), dynamic light scattering (DLS), zeta potential (ζ, ZP), and fluorescence spectroscopy. Furthermore, these AuNPs were functionalized with N-(3-dimethylaminopropyl)-N′-ethylcarbodiimide hydrochloride (EDC) and N-hydroxysuccinimide (NHS) to prepare modified carboxylated AuNPs. For bioconjugation with *Brucella* rOmp28 IgG pAbs, antibody-conjugated functionalized AuNP constructs were prepared and characterized using FT-IR analysis with strong N–H deformations. Subsequently, these bioconjugated AuNPs were used to develop a direct-differential slide agglutination assay with a detection limit of 10^4 CFU mL^{-1}. The sensitivity of this assay was compared with standard double-antibody sandwich ELISA (S-ELISA) using rOmp28 IgG pAbs with an LOD of 10^3 CFU mL^{-1} and a detection range of 10^2–10^8 CFU mL^{-1}. No intraspecies cross-reactivity was observed based on evaluation of its specificity with a battery of closely related bacterial species. In conclusion, the increased sensitivity and specificity of the developed agglutination assay obtained using bioconjugated functionalized AuNPs is ≥ 98% for the detection of *Brucella*. Therefore, it can be used as an alternate rapid method of direct WC detection

of bacteria as it is simple, robust, and cost-effective, with minimal time of reaction in the case of early disease diagnosis.

KEYWORDS

Brucella, agglutination assay, rOmp28, gold nanoparticles, outer membrane protein, polyclonal antibody

1 Introduction

Brucellosis is an endemic, mostly neglected but re-emerging, bacterial zoonosis; it mostly affects the world's low-income and low–middle income countries (Lemos et al., 2018; Bagheri Nejad et al., 2020). Its infection is spread by small, aerobic, intracellular, facultative, Gram-negative coccobacilli bacteria of the genus *Brucella*, and is considered one of the most economically important public health concerns (Bakri et al., 2018; Jansen et al., 2020). Brucellosis was propounded for the first time by Sir David Bruce on military campaigns in Malta, predominantly in the central Mediterranean region along with Sir M. Louis Hughes and Themistocles Zammit (Sayer, 2016). Sir Zammit explored the association of this disease with the consumption of raw milk from naturally infected goats and discovered its route of transmission (Wyatt, 2013). This disease is prevalent worldwide, mainly occurring in Central Asia and the Middle East; it is also widespread in South Asian countries such as India, China, Pakistan, and Sri Lanka, with sero-positive cases of human brucellosis mostly in agro-farmers, veterinary professionals, slaughter houses, and dairy workers (Guan et al., 2018; Xu et al., 2020). The four main species of *Brucella* (*Brucella abortus*, *Brucella melitensis*, *Brucella canis*, and *Brucella suis*) are well-known for their sustained endemicity, wide distribution, and prolonged systemic cases of Brucellosis in both domestic and wild hosts (Olsen and Tatum, 2016; Olsen et al., 2018; Yagupsky et al., 2019). On infection with brucellosis, livestock suffer from reduced milk production followed by frequent abortions, still births, retained placental lesions, vesiculitis, orchitis, epididymitis, and life-time sterility (El-Sayed and Awad, 2018; Khan et al., 2020). In humans, the symptoms include high undulant fever of unknown origin (FUO), focal complications with severe flu-like symptoms, fatigue, myalgia, neurobrucellosis, hepatosplenomegaly, loss of appetite, premature delivery, arthritis, septicemia, and destructive localized spinal infections (Rubach et al., 2013; Khan and Zahoor, 2018; Ukita et al., 2021). *Brucella* infection in humans is transmitted through consumption of unpasteurized milk, raw or undercooked meat, and infected animal by-products (MusallamAbo-Shehada et al., 2016; Holt et al., 2021). Occupational hazards and environmental disease reservoirs also propagate brucellosis infection in agriculture-based pastoral communities (Galinska and Zagorski, 2013; Shi et al., 2021). The transmission of bovine brucellosis is rapid, debilitating, and most prevalent in areas dominated by animal husbandry, and, because of its complex treatments in the absence of specific vaccines for humans, *Brucella* has become a candidate agent of major bioweapons (Pappas et al., 2006; Boggiatto et al., 2019; Yagupsky et al., 2019). For proper control and prevention of increased cases of brucellosis, serological surveillance, bacteriological investigation, immunoassay-based detection, and alternate diagnostic methods are deliberately used in screening acute and chronic cases (Lalsiamthara and Lee, 2017). The improper clinical management and misidentification of *Brucella* also contribute to the relapse of infection (Etemadi et al., 2019). Several tests which are based upon serological implications and its characterization are routinely used to test *Brucella*-related infection such as serum tube agglutination test (SAT), Rose Bengal plate test (RBPT), enzyme-linked immunosorbent assay (ELISA), 2-β mercaptoethanol test (2 ME), complement fixation test (CFT), and Brucellin skin test (BST) (Yohannes et al., 2012; Moreno et al., 2022). Direct slide agglutination assays are sensitive, cost-effective, rapid, and simple in terms of facilitating users with less expertise and require minimum time for multiple-sample testing (Saxena, 2012; Saxena and Kaur, 2013; Purwar et al., 2016). Such types of serological tests for the diagnosis of brucellosis in bovines, caprines, and ovines explore common surface antigens present in different species and strains of *Brucella* (Ghazy et al., 2016; Govindasamy et al., 2021). The sensitivity of the standard agglutination test was reported to be 95.6 %, with a specificity of 100 % at 1/320 antibody dilution using the standardized set of *Brucella* antigens (Memish et al., 2002). Also, in another study, the sensitivity and specificity of the immunocapture agglutination assay were reported to be 90.6%, with 94.2 % of negative predictive values determining the blocking antibodies in preliminary diagnosis of *Brucella* (Ozdemir et al., 2011). A rapid slide agglutination test using latex beads coated with four recombinant antigens of *Brucella* as potential biomarkers was reported to offer high specificity in serodiagnosis of canine brucellosis (Watarai et al., 2007). Moreover, the Centers for Disease Control and Prevention (CDC) has also recommended the use of *Brucella*-specific agglutination methods for further advent confirmations of serologically tested positive samples and all equivocals which are parallely screened by enzyme immunoassay (EIA) (Centers for Disease Control and Prevention (CDC), 2005). Therefore, a combination of available potential serological and molecular tests along with rapid agglutination assays can facilitate specific detection of *Brucella* with no time delay in cases of early clinical emergency (Al Dahouk and Nockler, 2011; Di Bonaventura et al., 2021; Lukambagire et al., 2021; Suo et al., 2021). Significantly, the primary and secondary polyclonal antibodies (pAbs) specific to immuno-dominant cellular antigens of *Brucella* can also be utilized efficiently in conjugation with various nanoparticles and functionalized biosensors for *Brucella* species-level detection in clinical samples (Baltierra-Uribe et al., 2019; Taheri et al., 2020). The active adsorption of specific IgG pAbs and monoclonal antibodies (mAbs) onto functionalized nanoparticles enhances the rate of agglutination reaction and antigen–antibody binding avidity due to multivalent effects (Choktaweesak et al., 2016; Busch et al., 2019). Recently, an immuno-chromatographic test system was developed for rapid serodiagnosis of *Brucella* based on the application of gold nanoparticles and quantum dots for detection of low but diagnostically significant titers of specific antibodies in revealing sub-clinical stages of brucellosis (Sotnikov et al., 2020). Another potential colorimetric immunoassay was developed for prompt detection of *Brucella abortus* using immunosensors conjugated with pAbs on activation, with 1-ethyl-3-(3-dimethylaminopropyl)-carbodiimide (EDC) and N-hydroxysuccinimide (NHS) as efficient detection probes (Shams et al., 2019). pAbs were conjugated with quantum dots, and

modified magnetic beads along with gold nanoparticle-screen printed carbon electrodes were shown to detect *Brucella* at 10^2 and 10^5 CFU mL^{-1}, respectively (Wu et al., 2013; Song et al., 2017). When such modified approaches were applied together with a sandwich immunoassay, successful detection of *Brucella* antibodies from multiple test serum samples was achieved (Li et al., 2017). Although the gold standard, known for early disease diagnosis, potentially relies on the propagation of bacterial cell culture, the use of specific isolation techniques and culture-based methods are very laborious, time-consuming, not used routinely, not cost-effective, methodologically complex, and requires highly skilled technical subject experts for handling of infectious live cultures (Sagi et al., 2017; Santos et al., 2021). The new approach of developing test methods based on specific antigen–antibody conjugation with metallic nanoparticles is conversely more reliable, efficient, and robust for low pathogen detection (Malaspina et al., 2017; Lin et al., 2021). Functionalized bioconjugated AuNPs exhibit unique optical properties that not only improve biosensing technology but also the specificity of antigen–antibody interactions for the development of rapid on-field detection assays (Tripathi and Driskell, 2018; Okyem et al., 2021). Moreover, the performance of commonly used ELISAs, to overcome existing challenges associated with sensitivity and stability, can be improved by exploring the unique physical and chemical properties of metal oxide nanoparticles (Gao et al., 2020). One such modified test method is a hybridization assay; the use of conjugated metal nanoparticles resulted in sensitive detection of *Brucella* up to 10^3 CFU mL^{-1} during direct visual detection of specific DNA sequences (Pal et al., 2017). In recent reports, the efficacy of anti-spike antibody and 4-aminothiophenol-conjugated gold nanoparticle-based SERS was newly demonstrated for detecting low concentrations of such microbiological viral antigens (1,000 virus particles per mL) within 5 min (Pramanik et al., 2021). Recently, in the case of *Brucella*, reduced limits of detection were observed with a new version of rapid vertical flow technology that can detect 4 IU mL^{-1} of the *Brucella* antibody as the experimental lower limit, with gold nanoparticles treated with β-cyclodextrin as a reducing agent (Fang et al., 2022). Also, a lateral flow immunoassay (LFA) strip test using anti-*Brucella* pAbs conjugated with colloidal AuNPs was reported, which can detect 10^7 CFU mL^{-1} of inactivated whole cells of *Brucella abortus* S99 (Prakash et al., 2021). In the present study, we functionalized and conjugated AuNPs to *Brucella* species-specific recombinant outer membrane protein (rOmp28)-derived mice IgG pAbs for enhancing the specific binding of avid antigen–antibody complexes by employing a rapid direct-differential slide agglutination assay in the predominant whole-cell detection of *Brucella*. The developed assay is highly sensitive and specific, with minimal time of reaction, and can be deployed in both field-based and clinical applications for screening multiple sample matrices concomitant to animal and human brucellosis.

2 Material and methods

The present study includes the preparation and functionalization of AuNPs prior to bioconjugation with mice IgG pAbs derived from *Brucella melitensis* 16M-specific recombinant outer membrane protein (rOmp28) for developing a direct-differential slide agglutination assay as shown in the schematic (Figure 1). Initially, the assay was optimized for sensitivity with a detection range and limit of detection (LOD) of 10^1–10^8 CFU mL^{-1} with two standard species of *Brucella* (*Brucella melitensis* 16M and *Brucella abortus* S99); there was further screening with a total of 36 clinical isolates and nine other standard strains of *Brucella* at the lowest LOD of 10^4 CFU mL^{-1}. The specificity of the assay was evaluated by a cross-reactive study with 26 other bacterial species closely related to *Brucella*. Validation of the experimental assay was performed by direct-slide agglutination of spiked whole cell (WC) Ags of *Brucella* in both clinical (urine and serum) and non-clinical (raw-milk) sample matrices. Furthermore, the specific potential efficacy of rOmp28-derived mice IgG pAbs was evaluated using earlier optimized double-antibody sandwich ELISA (S-ELISA) for WC detection of *Brucella* at an experimental LOD of 10^3 CFU mL^{-1} with a detection range of 10^2–10^8 CFU mL^{-1} (Hans et al., 2020).

2.1 Chemical reagents

The reagents used in thus study were chloroauric acid trihydrate ($HAuCl_4.3H_2O$, from Sigma-Aldrich, 520918), trisodium citrate dihydrate (Hi-media, GRM 1415), citric acid (Sigma, 251275 BCBZ1757), sodium borohydride (Sigma, 452874), Milli-Q Water (Milli-Q Direct 8, Millipore Unit), bovine serum albumin (BSA from Hi-media RM 105), fetal bovine serum (FBS from Hi-media, RM10409), *Brucella* selective supplements (BSS from Hi-media FD-005, 0000077461), *Brucella* selective broth (BSB from Hi-media, M348), brain–heart infusion broth (BHI from Hi-media, M210), Luria–Bertani broth (LB from Hi-media, M1245), protein-A antibody purification kit (PROSEP-A Montage-Millipore, United States, LSK2ABA20 AK082402), N-(3-dimethylaminopropyl)-N′-ethylcarbodiimide hydrochloride (EDC Sigma Ultra from Sigma-Aldrich, E–1769, 037K07536), N-hydroxysuccinimide (NHS from Sigma-Aldrich, 130672, BCBF1078V), O-phenylenediamine dihydrochloride (OPD from Sigma, 030153, 012-146-008), isopropyl β-D-1-thiogalactopyranoside (IPTG from Sigma, I6758, 056M4040V), iso-propanol (iso-propyl alcohol from Qualigens Fine Chemicals, 26895, NL17386305V), kanamycin sulfate (antibiotic from Sigma, K1377, SLBB0945V), Ni-NTA gel (Superflow from Qiagen, 30430, 154016665), polyclonal goat and rabbit anti-mice immunoglobulins/HRP (P0447, 20083051 and P0260, 20079831 from Dako Denmark), polyclonal goat anti-rabbit immunoglobulins/HRP (P0448, 20083037 from Dako Denmark), sodium azide (Sigma-Aldrich, S2002), urea (Sigma, U5378, 118K0087), methanol (Thermo-Fisher Scientific, 32407, 1,128/3 7109–6), phosphate buffer saline (PBS, pH 7.2, 10 mM L^{-1} from Sigma, P4417, SLBS1525V), hydrochloric acid (0.01 M HCl (Sigma, H1758), and 16-mercaptohexadecanoic acid (99 % MHA from Sigma-Aldrich, 674435).

2.2 Preparation of sol–colloid gold nanoparticles

The AuNPs were synthesized through a chemical reduction method (citrate synthesis) using gold tetrachloride trihydrate ($HAuCl_4.3H_2O$) as a starting material. The citrate synthesis (sol preparation) of AuNPs was performed by using the conventional and reproducible "Turkevich method" with slight modifications as described by Turkevich et al. (1951) and Laaksonen et al. (2006). Different concentrations of the starting material were used and optimized to obtain particles 50 nm in size at a constant volume of solvent (20 mL sterile Milli-Q water) and a

10.3389/fnano.2023.1132783

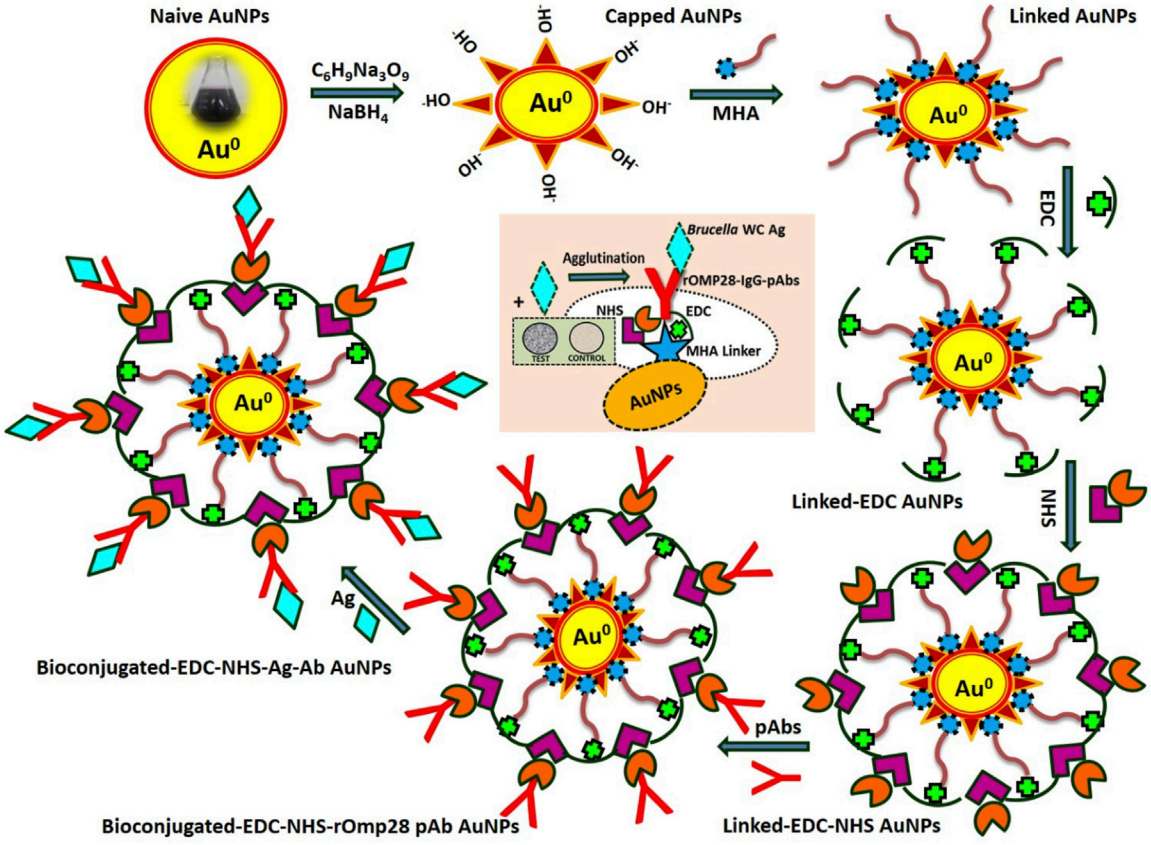

FIGURE 1
A complete scheme representing the methodology applied for development of agglutination assay using modified, functional, and bioconjugated AuNPs.

TABLE 1 Different rational concentrations of gold tetrachloride trihydrate (chloroauric acid, $HAuCl_4.3H_2O$) as a precursor material were used in the preparation of spherical sol–colloid nano-metallic AuNPs. Wine-red colored ruby-red tinted nanosize particles were inferred at an optimized concentration of 0.073 mM (<0.1 mM) with a particle size of 50 nm, prepared using a constant volume of solvent for 10–15 min (particle size analyzed by UV/Vis and TEM analysis).

Sample batch ID	Volume (solvent MQ in mL)	H (mL) $AuCl_4.3H_2O$ (Molarity in mM)	H (mM) $AuCl_4.3H_2O$ (in µL)	$HAuCl_4.3H_2O$ (in mg)	Trisodium citrate dihydrate (v/v)	Heating time (in min.)	Inference (color change)
A	20	0.990	2.71	8.67	2 mL 1% solution	10-15	Violet
B	20	0.990	2.71	8.67	Citric acid buffer A (50 % citrate + 50 % citric acid)	10-15	Yellowish orange
C	20	0.990	2.71	8.67	Citric acid buffer B (75 % citrate + 25 % citric acid)	10-15	Dark violet
D	20	0.990	5.4	15.606	2 mL 1% solution	10-15	Greyish violet
E	20	0.490	1.35	3.901	2 mL 1% solution	10-15	Dark violet
F	20	0.366	1	2.890	2 mL 1% solution	10-15	Crimson red
G	20	0.183	0.5	1.445	2 mL 1% solution	10-15	Dark red
H	20	0.073	0.2	0.578	2 mL 1% solution	10-15	Wine red
I	20	0.036	0.1	0.289	2 mL 1% solution	10-15	Orange red

fixed time of heating (10–15 min), as mentioned in Table 1. Glassware used in the preparation of AuNPs was first treated with aqua regia and washed at least thrice with triple distilled water (DW). After washing, glassware was sterilized with steam autoclaving (121°C for 15 to 20 min at 15 lbs pressure) using a Sanyo Labo Autoclave, MLS-3780, and hot-air dried (at 50°C) using a Labcon, FSIM Standard Incubator. For single-batch preparation of carboxylated AuNPs (thiol-linked AuNPs), 5 µL $HAuCl_4.3H_20$ (0.073 mM) prepared in 10 mL sterile milli-Q water was added to 200 mL ethanol (50 %) solution containing 0.3 mmol MHA at a boiling temperature of 100°C (Ellis et al., 2008; Hashemi et al., 2019). To this boiling solution (light pale-yellow colored), 2 mL freshly prepared 1 % solution of trisodium citrate dihydrate (capping agent) was added, and the obtained solution was allowed to cool to room temperature (Khashayar et al., 2017). The citrate reduction of gold resulted in the formation of AuNPs in sol–colloid form. After cooling, the pH value of the gold sol–colloid was measured [EUTECH pH-meter, Fisher Scientific, INDIKROM Papers (pH 1.0 to 14.0)] and was found to be in the range 6–8 (see Supplementary Figure S1). Thereafter, 20 mL freshly prepared aqueous solution of sodium borohydride (380 mg) was added as a strong reducing agent in order to further reduce the gold (Jurkin et al., 2016; Karimi et al., 2019). The aforementioned solution containing capped carboxylated AuNPs in MHA was continuously stirred (Magnetic Stirrer Spinot, Tarsons) for another 5 h at a constant speed of 200 rpm and was then allowed to precipitate at the bottom of the flask. These precipitated thiol-linked nanoparticles were washed using high speed centrifugation (15,000 to 20,000 rpm for 30 min) and vacuum-dried (Jouan RC 10.22, Thermo Fisher Scientific) for another 7–8 h for further characteristic analysis.

2.3 Characterization of synthesized AuNPs

Functionalized AuNPs were characterized by using UV-visible (UV-2450 Shimadzu), FT-IR (Perkin Elmer, Model Spectrum Two), and Raman spectroscopy (Renishaw Invia Raman Microscope, Gloucestershire, United Kingdom) to determine their optical properties and functional group. Analysis of the NPs' chemical nature, size, structure, surface morphology, and elemental composition was performed with XRD (Rigaku, fifth Generation Mini Flex 600 with Cu-Kα 1 radiation), SEM-EDX (HR FESEM, ULTRA Plus Model with EDX), and TEM (JEOL 1230) along with selected area electron diffraction (SAED). For obtaining the net surface charge, particle size distribution, quantitative binding stoichiometry, and bioconjugation stability of the functionalized AuNPs, apparent ZP (ζ) zeta potential (Nano-ZS, MALVERN Zetasizer Nanoseries, Software Version 7.11) and dynamic light scattering (Nano-ZS Zetasizer, MALVERN) analyses were performed. In parallel, serial UV-vis spectrophotometry (IMPLEN NanoPhotometer, Version 7122 V1.6.1) and fluorescence spectroscopy (PerkinElmer LS-55, Software FL WinLab™) for binding sensitivity and specificity were critically monitored to determine the accuracy of NP modification.

2.4 Bacterial strains and culture growth condition

In this study, nine standard strains of *Brucella* species (Supplementary Table S1), 26 *Brucella* closely related intraspecies (Supplementary Table S2), 36 human *Brucella* clinical isolates from different geographic regions of India (Supplementary Table S3), and a rOmp28-positive clone (*Escherichia coli* BL-21 clone) maintained in 30% glycerol (stored at −80°C) in the laboratory were used (Barua et al., 2016). Bacterial cultures were grown in BSB and BHI growth media with suitable supplements (BSS and 5 % FBS) incubated at 37°C inside a gyrating shaker incubator (Labcon 5081U shaking incubator from Labcon, United States) at a constant shaking speed of 180 rpm. The *Escherichia coli* BL-21 positive clone was grown in LB media supplemented with kanamycin sulfate (50 µg mL^{-1}) antibiotic selection. The handling of pathogenic bacteria and research work associated with this study was performed in a high-containment facility (HCF, DRDE-DRDO Gwalior, India) in the laboratory, following all the standard operating procedures and regulatory methods.

2.5 Cloning, expression, and purification of the recombinant outer membrane protein

A positive clone for the expression of the rOmp28 protein was obtained from the established bacterial molecular cloning-amplified clones, which was done earlier in our laboratory as described (Thavaselvam et al., 2010). The *Omp*28 gene (753bp) of *Brucella melitensis* 16M was PCR amplified, digested, and ligated using the pET-28a expression system. The *Escherichia coli* BL-21 (DE3) expression host was transformed with pET-28a (+) plasmid, and a bacterial culture for the positive recombinant clone was grown with kanamycin (50 µg mL^{-1}) antibiotic selection. The colony-PCR confirmed positive clone was induced with 1 mM IPTG at 5 h for recombinant protein expression. Furthermore, bacterial cells were lysed under denaturing conditions (urea) for rOmp28 protein purification with His-tag binding Ni-NTA gel filtration in Ni-NTA Gel Superflow for affinity column chromatography using different pH buffers [lysis buffer (pH 8.0), wash buffer (pH 6.3), and elution buffer (pH 4.5)]. The purified rOmp28 protein was dialyzed for desalting with subsequent changes in 6 M, 4 M, and 2 M urea buffer followed by sterile 1X PBS (pH 7.2) and was further estimated for protein analysis using the Folin–Lowry method and first dimension SDS PAGE gel electrophoresis (Lowry et al., 1951; Laemmli, 1970).

2.6 Animal immunization for pAb production and IgG purification

For generation of rOmp28 protein antigen (Ag)-derived IgG pAbs, a total of 12 BALB/c female mice were immunized. For animal dosing, 50 µg of Ag per dose per mice was administered at an interval of 1 week over a period of 2 months with six booster doses completed: day 0 (control bled for pre-immune sera, PIS), day 7 (priming with complete Freund's adjuvant, CFA), and day 14 to 49 (boosters with incomplete Freund's adjuvant, IFA) (Zhang et al., 2015). For the estimation of antibody (Ab) titer, whole blood collected from immunized animals was incubated at 37°C for 1 h and centrifuged at 5,000 rpm for 5 to 10 min at 4°C to obtain the hyper-immune sera (HIS) supernatant. Mice IgG pAbs were affinity purified with Montage protein-A columns as per the instructions of the antibody purification kit (Montage-Millipore, United States) and further analyzed using ELISA, SDS-PAGE, and

immunoblotting as per methods previously described (Hans et al., 2020). The antibody titer was estimated using indirect-ELISA whereby, rOmp28 protein Ag at a concentration of 20 μg mL^{-1} was suspended in sodium carbonate–bicarbonate coating buffer (0.05 M, pH 9.6) and immobilized on ELISA immuno-modules (Thermo-Nunc F8 Loose Maxisorp Immunomodules, 469949, 127747) for overnight (O/N) incubation at 4°C. Modules were washed with PBS/PBS-T thrice and blocked with 2% BSA O/N at 4°C, and ELISA was performed as detailed previously (Hans et al., 2020). The total yield of the purified IgG antibody obtained was 6 mg mL^{-1} and was analyzed by SDS-PAGE. The aliquoted purified antibody was stored at −20°C until further use.

2.7 Bioconjugation with functionalized AuNPs

Functionalized AuNPs were prepared by one-step EDC/NHS coupling with linked AuNPs, and then, they are conjugated to mice IgG pAbs according to the reported method with slight modifications (Zhao et al., 2004; Hashemi et al., 2019). To 5 mL of sterile 1X PBS (pH 7.2, 10 mM L^{-1}) containing 0.25 gm EDC (1.3 mM) and 0.25 gm NHS (2.2 mM) in a 1:1 ratio, 0.1 gm of prepared carboxylated-linked AuNPs and 0.002 gm of purified IgG pAbs were added (Busch et al., 2019). The solution was stirred slowly at 100 rpm for approximately 45 min at room temperature (RT). To this buffer solution, 3% bovine serum albumin fraction-V was added, and the solution containing bioconjugated AuNPs was centrifuged and washed twice in 10 mM PBS. The supernatant with unbound pAbs was removed, and conjugates were resuspended in 10 mM PBS. For small working test batches, 0.1 mL (100 μL from 6 mg mL^{-1} IgG pAb suspended in 10 mM PBS, stored with 0.3 gm of sodium azide as preservative) PBS containing 600 μg pAbs and 30 mg modified carboxylated-linked AuNPs were added to 1.5 mL 10 mM PBS solution containing EDC and NHS. For development of the agglutination assay, an optimized 50:1 ratio for active bioconjugation of AuNPs and IgG pAbs resulted in maximum stability of the conjugated pAbs. Increased concentration of the pAbs can hinder the orientation on the nanoparticle surface and can resist binding of the whole-cell antigens. For analysis of the conjugated pAb stability, FT-IR and optical intensity of conjugation were measured. Also, toxicity evaluation of the conjugated constructs was performed with validation studies using spiked clinical samples without any test analytes, for testing the performance of clinical matrices prior to agglutination. On conjugation, the functionalized bioconjugated material was subjected to characterization using FT-IR analysis.

2.8 Slide agglutination of WC *Brucella* using pAb-conjugated AuNPs

For development of the direct-differential slide agglutination assay, one drop (50 μL) from each of the prepared AuNPs-conjugated IgG pAbs and 10-fold serial dilutions of WC Ags (10^8 to 10^1 CFU mL^{-1} in 1X PBS) of *Brucella* at a 1:1 ratio were applied on the test slide. During positive reaction, visible aggregated clumps of WC particulate Ag and Ab complexes appeared on active immuno-agglutination. Such a direct agglutination was considered a positive test for the applied WC Ag. The detection range of agglutinated WCs in CFU mL^{-1} also indicated the experimental LOD for the developed assay.

2.9 Evaluation of assay sensitivity and specificity using inter- and intraspecies

For sensitivity and specificity of the developed assay, WC Ags at 1×10^5 CFU mL^{-1} of both inter- and intraspecies closely related to *Brucella* were tested, and the obtained results were analyzed. WC Ags of bacterial species for testing were mixed with AuNP-conjugated pAbs separately on test slides in a 1:1 ratio (50 μL each). The appearance of strong positive agglutinations during the test result revealed sensitivity, and the corresponding negative test result indicated specificity of the assay.

2.10 Assay validation for direct-slide agglutination in spiked matrices

For the purpose of assay validation, WC Ag at a concentration of 1×10^5 CFU mL^{-1} for two standard species of *Brucella* (*Brucella melitensis* 16M and *Brucella abortus* S99) was spiked in different clinical and non-clinical sample matrices. Then, 20 mL of unpasteurized raw-midstream cow and human milk, curdled with 5 mL of 10% citric acid prepared in 1X PBS, was diluted at a 1:1 dilution ratio in PBS. Furthermore, it was centrifuged at 6,500 rpm for 5 min, and the supernatant was used as the non-clinical sample matrix. Similarly, FBS and human sera (1:1,000 in PBS) along with morning midstream cow and human urine (1:1 in PBS) were used as clinical sample matrices. The results of the validation study indicated the AuNP-conjugated construct-related toxicity and direct potential efficacy of the developed assay in both clinical- and field-based applications.

2.11 Comparative S-ELISA for determining the test efficacy of rOmp28 IgG pAbs

The Sandwich-ELISA immunoassay was optimized for WC detection of *Brucella* in determining the specific test efficacy of rOmp28 protein-derived mice IgG pAbs, as described earlier by (Hans et al., 2020). The *Brucella* WC-derived rabbit IgG pAb (capture pAb at 10 μg mL^{-1}) and rOmp28-derived mice IgG pAb (detection pAb at 100 μg mL^{-1}), as optimized earlier using checker-board S-ELISA, were used for the developed assay (Hans et al., 2020). The sensitivity, detection range, and LOD of rOmp28-derived mice IgG pAbs for WC detection of *Brucella* using S-ELISA were determined to evaluate its test efficacy and its potential for the developed nanoparticle-based direct-differential slide agglutination assay in a clinical scenario.

2.12 Ethical Approval

This work was carried out at the Defence Research and Development Establishment (DRDE-DRDO), Ministry of Defence, Government of India, and was approved by the Institutional Animal Ethics Committee (No: 37/GO/Rbi/S/99/CPCSEA and IAEC MB-43/

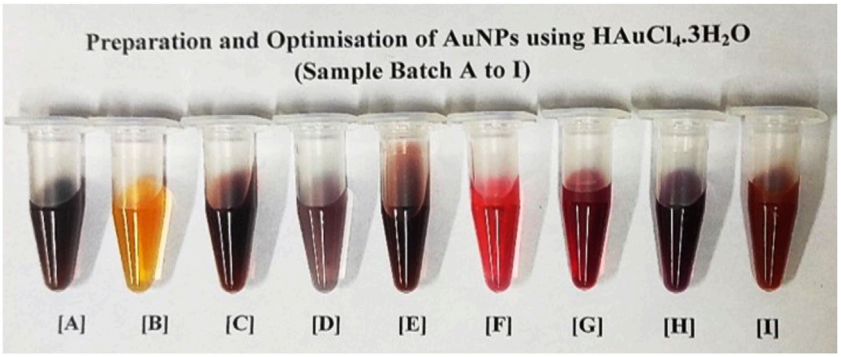

FIGURE 2
Batch-wise **(A–I)** sample preparation and optimisation of AuNPs at defined molar concentrations of gold precursor as shown in Table 1. Different batches of sol-colloids were obtained having **(A)** with violet, **(B)** with yellowish orange, **(C)** with dark violet, **(D)** with greyish violet, **(E)** with dark violet, **(F)** with crimson red, **(G)** with dark red, **(H)** with wine red and **(I)** with orange red colored nanoparticles. The batch sample 'H' with ruby-red wine color was standardized in bio-assay development for direct-rapid WC Ag agglutination of *Brucella* (concentration < 0.1 mM having particle size 50 nm).

57/DTS, dated: 14/06/2018 and IAEC BDTE-01/59/SP, dated: 05/06/2020) for the purpose of control and supervision of experimental animals. All the methods performed in this study were carried out in accordance with proper guidelines and regulations. The study was also approved by the Institutional Biosafety Committee of the Defence Research and Development Establishment (DRDE-DRDO), Ministry of Defence, Government of India vide protocol no. IBSC/15/MB/DTS/6.

3 Results

3.1 UV-visible spectrum analysis and measurement of the prepared AuNPs

Nanometallic AuNPs were prepared using sodium citrate and sodium borohydride as strong co-reducing agents (Haider et al., 2016). On reduction, gold Au^{3+} ions of $HAuCl_4.3H_2O$ were reduced to nano gold Au^0 and this was confirmed by the formation of wine-red sol–colloid with a ruby-colored red-tint at an optimized working concentration of 0.073 mM, which is almost < 0.1 mM of the precursor material (as shown in Figure 2). The particle size of AuNPs was controlled by optimizing the gold-to-citrate ratio as shown in Table 1. The synthesized naive monodispersed colloid particles (before capping) typically had a relative change in the particle size distribution range when analyzed by recording the mean absorbance of the samples. As a result of the analysis, corresponding absorbance spectra displayed a single absorption peak (λ_{max}) in the visible range between 510 and 550 nm (see Figure 3A). With the growth of particles, λ_{max} shifted toward longer wavelengths, and spherical-shaped nanoparticles appeared to have lesser eccentricities. The occurrence of this peak in the absorbance spectra was due to the effect of surface plasmon resonance (SPR). The increase in the SPR peak with the relative particle size of AuNPs was confirmed experimentally at an absorption peak value of 523 nm (see Figure 3A and Supplementary Figure S2A). The total band width of the prepared AuNPs indicated the energy band gap estimated by using the Tauc plot (Eq. 1) in a single particle spectrum, and was found to be 2.68 eV, attributed to the spherical shape of AuNPs (as shown in Figure 3B).

$$(\alpha \cdot h\nu) = A\left(h\nu - \mathrm{E}g\right)^m, \quad (1)$$

where α is the absorption coefficient, h is Plank's constant, ν is the incident photon frequency, A is the optical constant, E*g* is the band gap energy related to the particular transitions of a material, and m is the exponential factor, which depends on the nature of electron transitions and is equal to values 1/2 or 2 for direct or indirect transition band gaps, respectively (Makula et al., 2018).

3.2 Characterization of AuNPs with FT-IR and Raman spectroscopy

FT-IR spectra of modified (naive, capped, and linked) and functionalized AuNPs (bioconjugated-EDC-NHS-Ab AuNPs) were recorded in the wave number range of 4,000 cm^{-1}–450 cm^{-1}, and the results obtained were analyzed for the identification of functional groups (Figure 4A). Initially, for naive nanoparticles collected before reduction, absorption at 3,300–3,400 cm^{-1} corresponds to medium N–H stretching vibrations of hydrogen bonds in amines along with strong and broad bonds of the pendant hydroxyl (–OH) group of alcohols. Another sharp broad peak at 2,500–3,300 cm^{-1} originated from strong O–H stretching of pendant carboxylic acid and weak S–H stretching of thiols (Bartczak and Kanaras, 2011; Dey et al., 2018). Also, the absorption peaks at 1,640 cm^{-1} and 1,403 cm^{-1} of AuNPs are ascribed to strong C=O stretching vibrations of amides, C=C stretching of monosubstituted alkenes, carboxylic group, and relates to the sulfonyl chloride (Shikha et al., 2017). After the addition of reducing agents, capping of AuNPs occurs and medium to strong C–H stretching vibrations of the $-CH_2$ group are assigned to the 2,983 cm^{-1} absorption peak. The shift of peaks at relative position of 2,600–2,550 cm^{-1} is attributed to weak S–H stretching of the thiol group. The strong peak at 1,643 cm^{-1} relates to C=C stretching of monosubstituted alkenes and absorption at 1,250–1,275 cm^{-1} is assigned to C–O stretching of the alkyl aryl group along with corresponding O–H bending in capped AuNPs.

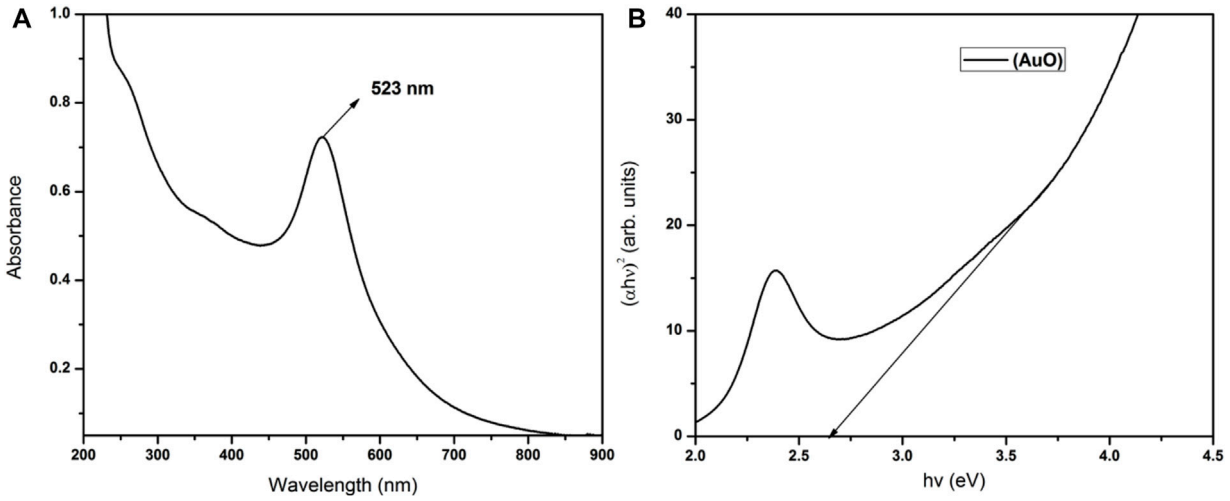

FIGURE 3
UV-visible analysis with **(A)** absorption spectra of AuNPs showing an optical absorption peak at λ_{max} 523 nm and **(B)** total optical absorption band width of reduced nanogold obtained using the Tauc plot showing the corresponding band gap energy at 2.68 eV, attributed to the relative size of AuNPs.

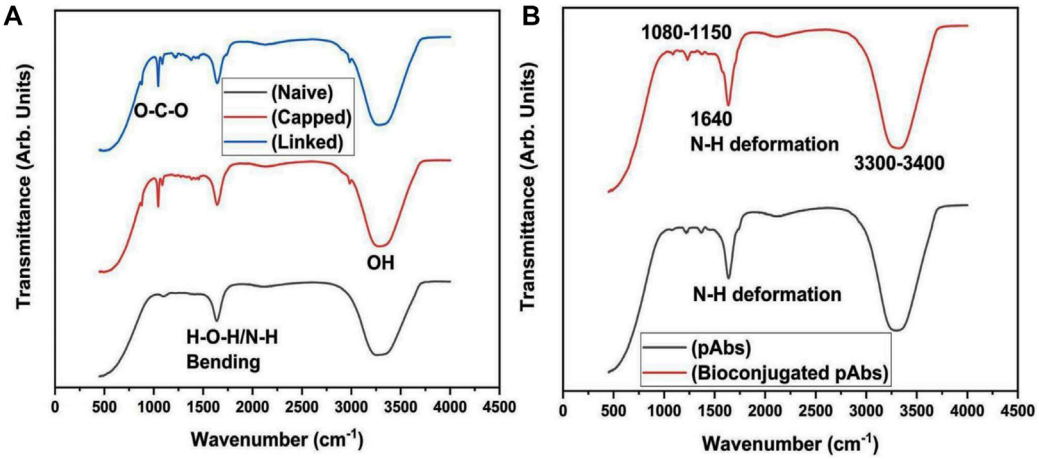

FIGURE 4
Characterization of AuNPs with **(A)** FT-IR analysis indicating N–H (3,300–3,400 cm^{-1}) stretching vibrations of amines, C=O (1,640 and 1,403 cm^{-1}), O–H (2,500–3,300 cm^{-1}), and S–H (2,600–2,550 cm^{-1}) stretching of amide, carboxylic, and thiol groups, C–O (1,250–1,275 cm^{-1}) stretching of alkyl aryl group and –OH bending of alcohols along with C=C (1,643 cm^{-1}), C–H (1,382 and 2,983 cm^{-1}), N–O (1,505 cm^{-1}), and CO–O–CO (1,044–1,085 cm^{-1}) stretching of carboxylic, alkanes and alkyl groups, nitro, alcohols and anhydride groups at different absorption peaks for naive, capped, and linked AuNPs and characterization of naive and bioconjugated pAbs (bioconjugated-EDC-NHS-Ab); **(B)** FT-IR spectrum analysis of naive pAbs with strong N–H (3,300–3,400 cm^{-1}), S–H, and S=O (1,400–1,300 cm^{-1}) stretching vibrations of amide, thiol, sulphonyl, and convoluted O–H groups. For antibody peptide bonds, stretching vibration peaks of C–N and C–O (1,500–1,650 cm^{-1}) along with strong N–H bending of amide groups were analyzed. In bioconjugated functionalized pAb, FT-IR analysis indicated enhanced stretching vibrations of S–H, N–H, and C–H bonds (3,300–3,400 cm^{-1}) for thiol and amide groups along with N–H and C=O (1,640 cm^{-1}), C–N, and N-H (1,230–1,330 cm^{-1}) bending vibrations, and C–O (1,080–1,150 cm^{-1}) strong stretching vibration of amides, amines, carbonyl, aromatic amine with analyzed sharp bending vibrations of N–H deformation for functionalized pAbs.

The relative peaks with corresponding shift in absorption at 1,505 cm^{-1}, 1,382 cm^{-1}, and 1,044 to 1,085 cm^{-1} are attributed to stretching vibrations of N–O of the nitro group, C–H bending of alkanes, and C–O stretching of alcohol along with strong bond CO–O–CO stretching of the anhydride of $NaBH_4$ as the hydride source, respectively (Muddapur et al., 2022). For linked AuNPs, MHA crystallinity on modified NPs can be monitored by a sharp and strong broad bond peak at 3,001 cm^{-1}, indicating N–H and C–H stretching of amine and alkyl groups of EDC and NHS along with the aforementioned peaks (Hinterwirth et al., 2013). Also, AuNPs generally exhibit superlative "surface enhanced Raman scattering (SERS)" properties which were analyzed by Raman spectroscopy (Khatoon et al., 2018). Raman spectra obtained for modified capped and linked AuNPs with corresponding bonds stretching are shown in Figure 5. In the presence of AuNPs, quenching of the fluorescence signal occurred, resulting in spectra with different peaks. Due to the light-scattering process, a change in energy (loss or gain) of the scattered photon at varied wavelengths corresponds to particular bonds in a

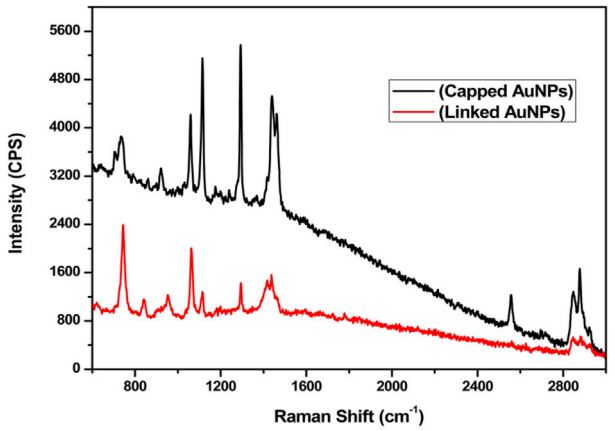

FIGURE 5
Raman spectroscopy (SERS) showing spectra of chemical bond stretching for C–H, S–H, C–H, N=N, C–O–C, C–C, and C–S at corresponding peaks of 2,845, 2,878, 2,556, 1,463, 1,440, 1,292, 1,114, 1,058, 921, 736, and 705 cm^{-1} for capped AuNPs and stretching vibrations of C–H, C=O, N=N, C–C, C–O–C, and C–S at enhanced peaks of 2,843, 1,723, 1,425, 1,294, 1,112.94, 1,063, and 744 cm^{-1} for linked AuNPs, respectively.

molecule. This spectral fingerprint is unique and defines a relative molecular structure of AuNPs based on the characteristic analysis of its physical properties. A 785 nm excitation wavelength laser beam was used. The bands located at 2,845, 2,878, 2,556, 1,463, 1,440, 1,292, 1,114, 1,058, 921, 736, and 705 cm^{-1} were assigned to strong C–H, S–H, asymmetric $–CH_2$ and $–CH_3$, aromatic N=N, asymmetric C–O–C, C–C, and C–S bonds stretching vibrations in capped AuNPs, respectively (Gorbachevskii et al., 2018). The three transient peaks at 1,292, 1,114, and 1,050 cm^{-1} are assigned to stretching vibrations of strong C–S and C–C, along with peaks at 736 and 705 cm^{-1} representing bending vibration of the C–S, indicating overlapping intensity of AuNP samples on active reduction. The enhanced peaks at 1,292 and 1,114 cm^{-1} correspond to aliphatic chain stretching vibrations of C–C and asymmetric C–O–C bonds, respectively. Due to the oxidation of citrate ligands in citrate-capped gold nanoparticles, amplification of SERS occurs, and in citrate-stabilized nanoparticles, citrate can be easily exchanged with –NH and –SH functional ligands (Piella et al., 2017). In the modified linked AuNPs, bands at 2,843, 1,723, 1,425, 1,294, 1,112.94, 1,063, and 744 cm^{-1} are attributed to strong C–H, C=O, N=N bond stretching, C–C bond aliphatic chain vibrations, asymmetric C–O–C, and aliphatic C–S and thiol bonds, as shown in Figure 5 (Madzharova et al., 2020; Aldosari, 2022). The bands located at 1,300 cm^{-1} and in the range 1,060–1,150 cm^{-1} can be associated with aromatic C–C band stretching and C–O–C, C=S stretching, C–H bending vibrations, respectively (Wei et al., 2019).

3.3 Powder X-ray diffraction analysis of AuNPs

On XRD analysis of the dried AuNPs, a pure crystalline structure of nanoscale particles was analyzed. The intense diffraction peaks at 2θ values 38.16°, 44.31°, 64.41°, and 77.50° correspond to the reflections of (111), (200), (220), and (311) set of planes, respectively, of a face-centered cubic (fcc) lattice, as shown in Figure 6 (Biao et al., 2018; Roddu et al., 2020). A peak at 56.32° along with other two peaks at 75° and 83.5° correspond to the orthorhombic phase of Au_2O_3 material [56.32° = (711), 75° = (113), and 83.5° = (333)], calculated from PCPDFWIN ICSD # 710579 (see Figure 6A). This revealed that in addition to Au, a small fraction of Au_2O_3 material is also present in naive gold nanoparticles. The defined sharpness of the peaks directly associates with the crystalline size of AuNPs. For a smaller crystallite size, the peaks are wide and for big crystallites, the peaks are sharper. The crystallite size was calculated by applying the Debye Scherrer formula, as shown in Eq. 2 (Zaman et al., 2019).

$$D = \frac{0.9\lambda}{\beta \cos\theta}, \tag{2}$$

where D is the average crystallite size, λ is the wavelength of the X-ray used, and β is the width at half maximum of the diffraction X-ray peak. This width of the peak and crystallite size had an inverse relation. The larger the crystallite size, the sharper the diffraction peak. In this XRD analysis, the crystallite sizes of naive, capped, and linked AuNPs are 10 nm, 13.5 nm, and 14.5 nm, respectively (as shown in Figures 6A–C). Therefore, the sharpness of the peaks follows the respective order: linked > capped > naive, and θ is Bragg's angle. The lattice parameter was calculated for all the three samples using the following formula for cubic systems:

$$\frac{1}{d_{hkl}} = \frac{h^2 + k^2 + l^2}{a^2}.$$

Also, the lattice parameters for naive, capped, and linked AuNPs samples were calculated to be 4.1 Å, 4.1 Å, and 4.09 Å, respectively, and are very close to the reported values (Busch et al., 2019). In capped AuNPs, aggregation of particles was prevented due to stearic hindrance and electrostatic repulsions introduced by the capping agents, preventing AuNP cementation which also affects the sharpness of peaks. On the contrary, in linked AuNPs, this intensity of sharpness is more intense and clear due to increased intensity and particle size at minimum agglomeration. The results, however, indicated that all the AuNPs were grown in a cubic crystal system of lattice.

3.4 Characterization of AuNPs with SEM and TEM-SAED imaging

SEM-EDX analysis was performed at an applied voltage of 20 keV, and a spectrum of pure gold atoms with spherical-shaped nanoparticles was analyzed (see Supplementary Figure S3). For TEM analysis, copper–carbon mesh grids were coated with a drop of AuNP colloid and mixed together with iso-propanol to reduce the surface tension. These grids loaded with test samples were dried for 20–30 min inside the vacuum chamber and analyzed for the results. The sizes of nanoparticles from TEM micrographs were found to be ~50 nm, ~64 nm, and 110 nm for naive, capped, and linked AuNPs, respectively (as shown in Figures 7A–C). On further analysis of the TEM-SAED pattern for naive AuNPs, bright spots with concentric circular rings for the (111), (200), and (220) set of planes of gold indicated the polycrystalline nature of the gold nanoparticles (Figure 7D). Therefore, at a lesser concentration of the gold precursor (0.073 mM < 0.1 mM) for the synthesis of AuNPs, more

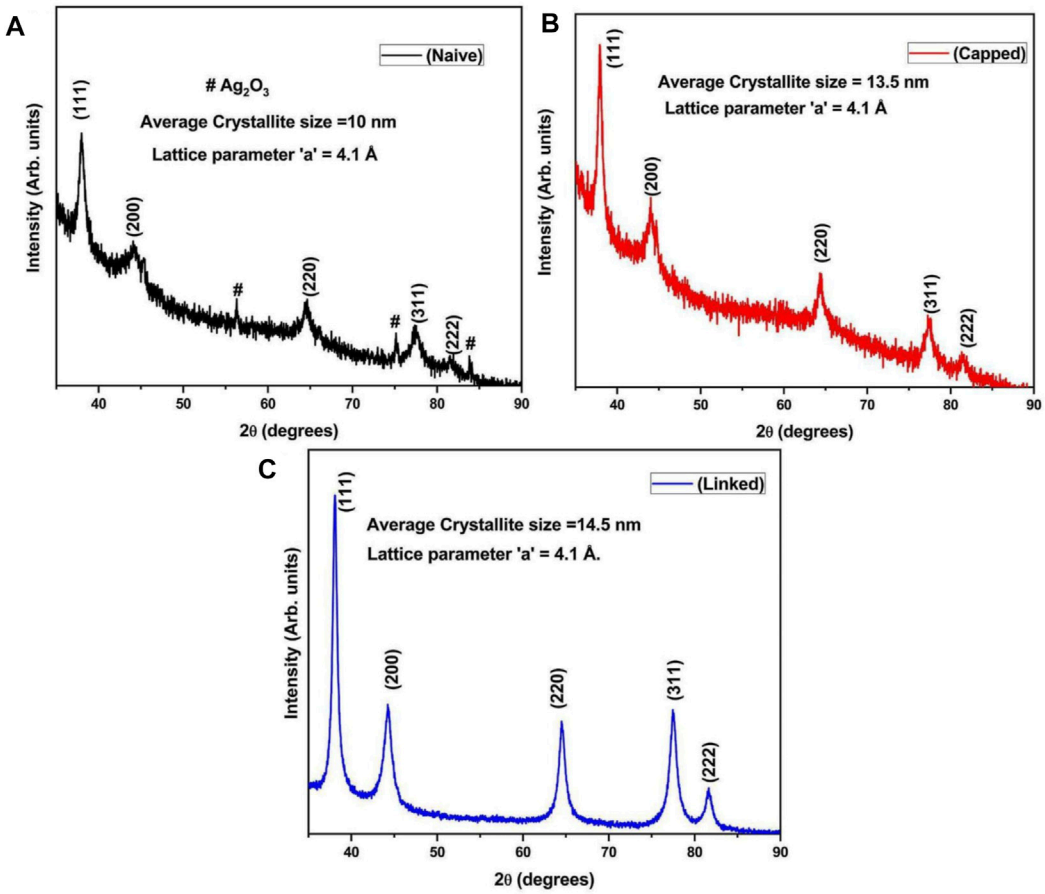

FIGURE 6
Characterization using powder-XRD with **(A–C)** XRD analysis showing angular diffraction peaks at 2θ values of 38.16°, 44.31°, 64.41°, and 77.50° with interplanar spatial reflections of the fcc crystal lattice at the (111), (200), (220), and (311) set of planes for naive, capped, and linked AuNPs. Diffraction peaks at 56.32°, 75°, and 83.5° corresponding to the orthorhombic phase of Au_2O_3 with spatial reflections of the fcc crystal lattice at the (711), (113), and (333) set of planes for naive and capped AuNPs. The parameters of the crystal lattice were obtained at 4.1 Å, 4.1 Å, and 4.09 Å at 10 nm, 13.5 nm, and 14.5 nm, respectively.

uniform, relatively identical, and small-sized spherical particles are obtained for stable bioconjugation (Ngo Thanh et al., 2016). Also, the synthesis and dispersion of nanoparticles in alcohol solution induced less aggregation than water and resulted in AuNPs with pendant carboxylic and alcoholic functional groups for strong bonding with Ab peptides.

3.5 Evaluation of NP surface charge and stable biomolecular binding with ZP (ζ) and DLS

For potential bioassay development, AuNPs were modified (viz., naive, capped, and linked AuNPs), and their step-by-step upgradation was critically monitored by measuring the zeta potential [at temperature 25°C with 12 (ζ) runs] of samples using deionized water (DI) as a dispersant in the zeta dip cell. The two-step citrate reduction of NPs shows a negatively charged surface at neutral pH. Also, on characteristic chemical linking with MHA, an increased negative surface potential was observed (ζ = −10.6 ± 7.25/−12.1 ± 3.42/−23.3 ± 5.01 mV for naive, capped, and linked AuNPs, respectively) due to covalent and site-specific thiol linking (see Supplementary Figure S4A,B; Supplementary Figure S5A,B,C). On functionalization of AuNPs with EDC and NHS, the relative ζ-potential further changed with respect to carboxylated NPs, and their biomolecular covalent binding during bioconjugation with pAbs further resulted in an increase of the net negative surface charge (ζ = −21.2 ± 5.35 and −22.8 ± 5.44 mV for linked-EDC-NHS and bioconjugated-EDC-NHS-Ab, respectively) as shown in Supplementary Figure S4C,D and Supplementary Figure S5D,E,F. On specific Ag-Ab interactions with bioconjugated-EDC-NHS-Ab AuNPs, adsorption of negatively charged rOmp28 protein Ag (depending on orientation of binding) on bioconjugated-EDC-NHS-Ab AuNPs having positively charged protein lysine residues experienced a positive shift in the ζ-potential distribution (ζ = −18.1 ± 4.97 mV from −22.8 ± 5.44 mV for bioconjugated-EDC-NHS-Ag-Ab from bioconjugated-EDC-NHS-Ab, respectively) as shown in Supplementary Figure S4C,D. The observed relative intensity (by phase, voltage, and current) of AuNP surface ζ-potential qualitatively increased with the potential drop of interaction and provided specific and sensitive affinity binding

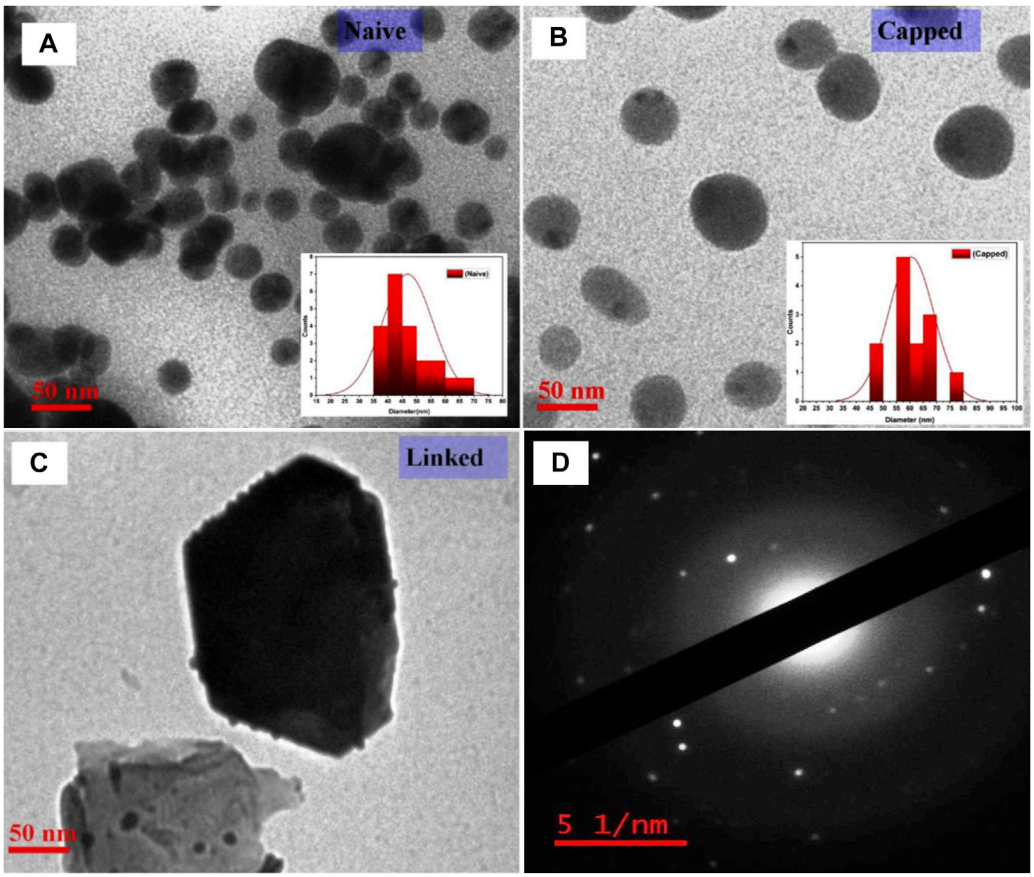

FIGURE 7
Characterization of AuNPs using TEM-SAED with, **(A–C)** TEM micrograph analysis indicating the sizes of the nanoparticles as ~50 nm, ~64 nm, and 110 nm for naive, capped, and linked AuNPs, respectively, with the relative shift in particle size on analysis by UV-vis spectroscopy, and **(D)** TEM-SAED showing patterns with bright spots of concentric circular rings (center to periphery) corresponding to the (111), (200), and (220) lattice planes of polycrystalline gold.

of antigenic sites with characteristic pAbs (see Supplementary Figure S6A–D). The specific orientation of available protein residues during biomolecular binding also increased the surface ζ-potential on NPs (Khashayar et al., 2017; Busch et al., 2019). The increased negative potential of AuNPs explained surface formation of pAb corona face-orientations (compared to less charged carboxylated NPs) for sensitive and stable Ag–Ab bioconjugations below the protein isoelectric point (pH ≤ 9), as shown previously in two different overlay combinations (viz., naive, capped, and linked combination and linked-EDC-NHS, bioconjugated-EDC-NHS-Ab, and bioconjugated-EDC-NHS-Ag-Ab combination). A key aspect for the formation of promising nanostructures is to control and characterize their physico-chemical parameters resulting in stable bioconjugates. Therefore, to determine such biomolecular orientation and nanosize distribution, modified AuNPs were characterized using the DLS analytical tool. Size distribution, both by intensity and volume, were observed with Zetasizer DLS [at a temperature 25°C with 60s–80s durations] using DI water as the dispersant in disposable sizing cuvettes. For every modified NP sample, a total of three DLS measurements with three consecutive test repeats against each measurement were performed, with an initial equilibration of 120 s. Furthermore, 10 μL mL^{-1} of each sample was measured from each batch (before and after bioconjugation of overlay combinations) of AuNPs in DI water against their respective pH of suspended buffer (see Supplementary Figure S1). DLS for mean hydrodynamic diameter and particle size was observed for two different overlay combinations (viz., naive, capped, linked and linked-EDC-NHS, bioconjugated-EDC-NHS-Ab, and bioconjugated-EDC-NHS-Ag-Ab). Also, DLS values obtained were found to be larger due to the presence of a double-layer effect of particle radius in solutions as compared to SEM/TEM analysis, which is obtained for dried powdered states of samples (Supplementary Figure S7) (Khashayar et al., 2017; Fernandez-Ponce et al., 2018). Hence, the resulting particle size distributions by intensity were observed to be 50.51 (d.nm) ± 23.20 (intensity 83.9 %), 106.7 (d.nm) ± 16.95 (94.3 %), and 112.2 (d.nm) ± 15.05 (100 %) for naive, capped, and linked AuNPs, respectively (see Supplementary Figure S7D; Supplementary Figure S8A–C). For the bioconjugated AuNP combination, the particle size distributions by intensity were observed to be 106.7 (d.nm) ± 15.54 (94.5 %), 233.2 (d.nm) ± 16.84 (100 %), and 262.5

(d.nm) ± 15.70 (100 %) for linked EDC-NHS, bioconjugated-EDC-NHS-Ab, and bioconjugated-EDC-NHS-Ag-Ab AuNPs, respectively (see Supplementary Figure S7C; Supplementary Figure S8D–F). Also, to predict the particle size distributions by volume, DLS of naive, capped, and linked AuNPs (before bioconjugation) were observed with Z-average = 428.2 (d.nm), having 100 % distribution by volume and linked AuNPs at a particle size of 108.9 (d.nm) ± 18.52 (d.nm) (see Supplementary Figure S7B).

3.6 Characteristic UV-Vis analysis and fluorescence spectroscopy of modified AuNPs

For the accuracy of bioconjugation and sensitive binding, modified AuNPs were analyzed at very low concentrations of NPs using fluorescence spectroscopy. Parallel to fluorescence, UV-visible analysis for nanoscopic characteristics, measurement of absorption peaks, and curve appearance were also observed. The shift in absorption peak determined the increase in particle size of NPs, and the absence of bands above 650 nm (wavelength range between 200 and 800 nm at a pathlength of 10 mm) wavelength indicated minimal aggregation of AuNPs. Likewise, for modified AuNPs, absorption peaks were observed at 523 nm with decreased absorbance values of 0.649, 0.461, and 0.097 for naive, capped, and linked AuNPs, respectively (see Supplementary Figure S2A–C). Therefore, it suggested that during two-step reduction (citrate-stabilized and borohydride co-reduction), surface hydrogen species were formed, which, on interaction with linking MHA (carboxylic acid-terminated with thiol heads), underwent ligand exchanges and conferred changes in the refractive index and dielectric constant to the AuNP surface (Willey et al., 2004; Pengo et al., 2017; Ansar et al., 2018). Due to electrostatic repulsion from surrounding negative citrate particles, SPR showed an absorption peak at 523 nm. Sodium citrate is an efficient capping agent; on the other hand, sodium borohydride is a strong reducing agent. This co-reduction was done purposefully to control the particle growth for bio-functionalization of AuNPs, since smaller nanoparticles are difficult to modify and often lead to bioconjugate toxicity. Therefore, to obtain biocompatible functionalized AuNPs with less reactivity toward clinical matrices (such as blood, serum, plasma, lymph, and body fluids), dual reduction of AuNPs was performed for stable agglutinations. Co-reduction in an aqueous solution favored a fast nucleation process and homogenous particle size growth and ripening (Piella et al., 2016; Fernandez-Ponce et al., 2018). The hydrodynamic diameters and particle size distributions for naive, capped, and linked AuNPs were measured by TEM and DLS methods and the results indicated the formation of spherical monodispersed AuNPs. In DLS, a higher proportion of homogenous particle sizes is appreciated with maximum size distribution. Furthermore, the decreased absorption value due to MHA-associated corona formation on the surface of AuNPs showed less electrostatic repulsions (Techane et al., 2011; Li et al., 2019). On the other hand, for bioconjugated AuNPs, absorption peaks were observed at a wavelength shift of 528 nm with corresponding absorbance values of 0.098, 0.306, and 0.291 for linked EDC-NHS, bioconjugated-EDC-NHS-Ab, and bioconjugated-EDC-NHS-Ag-Ab AuNPs, respectively (see Supplementary Figure S2D–F). This shift in the UV-vis absorption maximum of AuNP surface plasmon to a higher wavelength reflected an increase in the particle diameter (Suchomel et al., 2018). The bi-functional EDC-NHS functionalization was attributed to the formation of carboxylated AuNPs and, during bioconjugation with pAbs, resulted in corona face-off orientations on AuNPs with a stable net surface charge (Totaro et al., 2016; Busch et al., 2019). This further corresponds to an apparent increase in the absorption value with a relative drop after the interaction of a specific protein antigen by quenching F(ab)2 fragments of pAbs oriented on AuNPs. Therefore, the fluorescence of modified AuNPs was measured with nanochromators with an excitation range of 200–800 nm (with zero order selectable) and emission at 200–650 nm (a standard photo multiplier is zero order at 800–900 nm, with an optional R928 photo multiplier). The accuracy of the wavelength was ± 1.0 nm with a reproducibility of ± 0.5 nm (filter wavelengths 290, 350, 390, 430, 525 nm; a black shutter with 1% attenuator; and clear beam position) and the signal-to-noise ratio was 500:1 r.m.s (Raman band of water at excitation 350 nm and bandpath 10 nm). The samples were analyzed using a single position water thermostable holder for the quartz cuvettes. The emitted light (perpendicular to excitation) was collected by a spectrometer and calibration was performed by subtracting the spectrum of a blank sample (DI water with no AuNPs) from all the spectra of modified AuNPs (Zuber et al., 2015). In this study, a fluorescence peak at 619 nm was observed for naive, capped, and linked AuNPs, and a subsequent increase in the intensity of the peak at 621 nm was measured for each modified bioconjugated sample of AuNPs (1:15 ratio, 0.2/3 mL of DI water), as shown in Figure 8. It was observed that the intensity of the fluorescence peak increased for 50 nm naive AuNPs and was quantitatively enhanced further with increasing particle size at low concentrations of NPs. Similarly, it also decreases with a decrease in the particle size at high NP concentrations. The shift and high intensity of fluorescence peaks for modified AuNPs (naive, capped, and linked) during bioconjugation represented an increase in biomolecular binding on the AuNP surface (Figure 8).

3.7 Expression and purification of the *Brucella* recombinant rOmp28 protein

For the generation of IgG-pAbs to bioconjugate with AuNPs, the expressed rOmp28 protein was purified utilizing different pH-gradient buffer systems with His-tag binding Ni-NTA gel filtration affinity column chromatography, and a 32-kDa protein was obtained with a total yield of 3 mg mL^{-1} on purification (see Figure 9A). For animal immunization, 50 μg mL^{-1} of dialyzed rOmp28 protein was suspended in 1X PBS and administered in animals for production of rOmp28-derived IgG pAbs.

3.8 Production of pAbs against rOmp28 protein Ag

The antibody titer value ≥ 64,000 was obtained with I-ELISA using rOmp28 Ag as “immobilization Ag” on the ELISA test

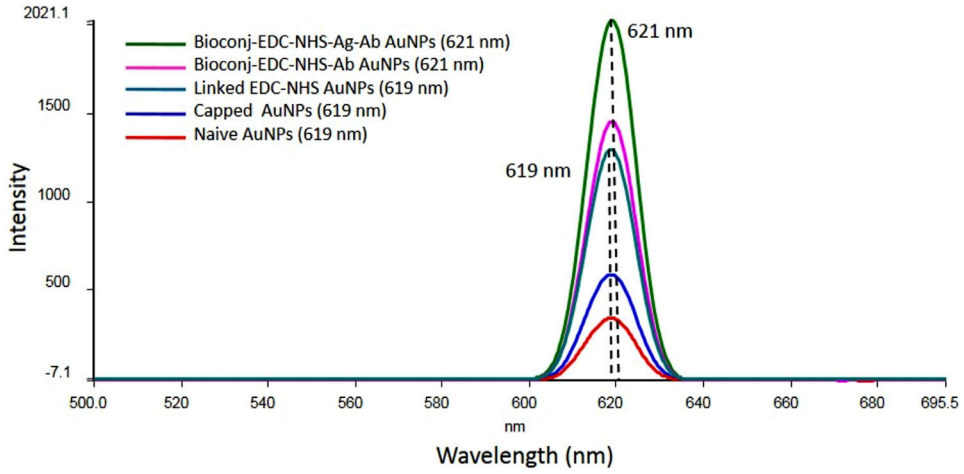

FIGURE 8
Fluorescence spectroscopy analysis of AuNPs showing the characteristic shift and an increase in the intensity of the absorption spectrum related to the surface plasmon resonance of naive, capped, linked, and bioconjugated AuNPs (bioconjugated-EDC-NHS-Ab and bioconjugated-EDC-NHS-Ag-Ab) with the corresponding peak shift from 619 nm to 621 nm. The increase in the intensity of the absorption maximum during step-by-step AuNP modification indicated selective detection of particles with a particular size and shape.

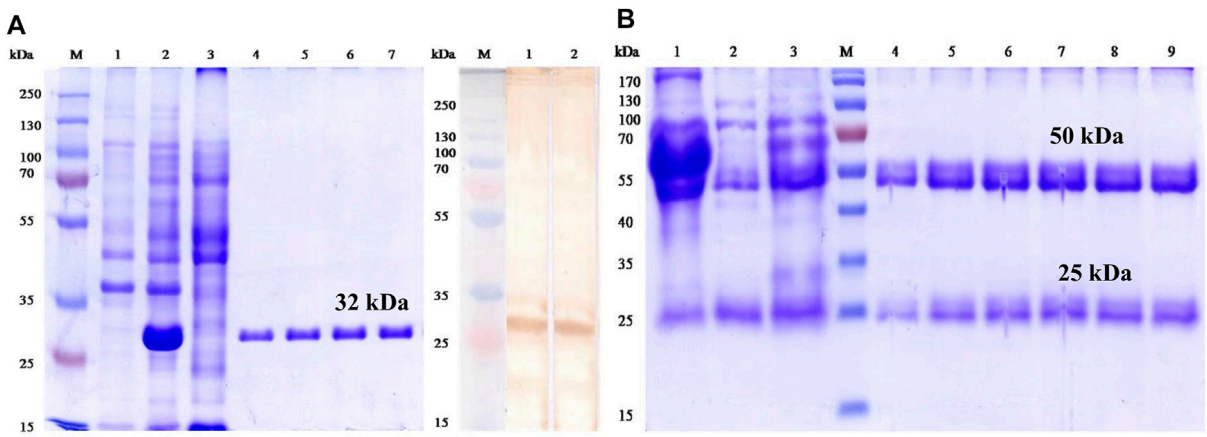

FIGURE 9
First-dimension SDS-PAGE and immunoblot analysis of rOmp28 Ag and IgG-pAbs, respectively, with **(A)** characterization of the expressed and purified rOmp28 protein of *Brucella melitensis* 16M using SDS-PAGE showing the purified recombinant protein of 32 kDa (molecular weight) without any impurity. PAGE analysis with un-induced (*Escherichia coli*, BL-21 clone) lysate (Lane 1), 1 mM IPTG induced (BL-21) clone for 5 h (Lane 2), Ni-NTA agarose column flow through (Lane 3), purified rOmp28 protein elutes 1 to 4 (Lane 4 to 7) in 8M urea at denaturing conditions, Lane M with Fermentas #SM1811 protein marker, and characteristic immunoblot analysis of the specific immuno-reactivity of rOmp28-derived mice IgG pAbs showing positive immunoblot with *Brucella melitensis* 16M rOmp28-purified protein antigen (Lanes 1 and 2) and Lane M with Fermentas #SM1811 protein marker, respectively. **(B)** SDS PAGE analysis of purified rOmp28 mice IgG pAbs developed against the rOmp28 protein antigen of *Brucella melitensis* 16M showing crude mice polyclonal HIS (Lane 1), column wash and flow through (Lane 2 and 3), purified mice IgG pAbs elutes 1 to 6 (Lane 4 to 9) and Lane M with Fermentas #SM0671 protein marker. On polyclonal IgG antibody purification, heavy (large) and light (small) chain fragments at 50 and 25 kDa molecular size, respectively, were obtained.

plates, as shown in Supplementary Figure S9. The antibody titer is defined as the "highest dilution that represents an absorbance greater than or equal to 2.1 fold of the background absorbance" (blank OD value/negative value) (Zhu et al., 2016). Also, a polyclonal regression co-efficient value (R^2) equal to 0.981 was obtained, with linearity in the data pattern and minimum low bias.

3.9 SDS-PAGE and immunoblot analysis of purified IgG pAbs

SDS-PAGE electrophoresis was run at 12% gel composition, and it revealed two fragments of IgG pAbs. One heavy chain fragment at 50 kDa and another light chain small fragment at 25 kDa were obtained on antibody purification (see Figure 9B). A total of 5 μg

lysed sample of IgG pAbs was applied on the SDS gel for analysis. On immunoblot analysis, a positive blot of 32 kDa protein, was obtained with rOmp28 IgG pAbs at 1:100 working dilution prepared in 1X PBS, as shown in Figure 9A. The immunoblot results revealed strong immuno-reactivity and immuno-affinity of the rOmp28 protein toward its purified IgG pAbs of BALB/c mice.

3.10 FT-IR analysis for "bioconjugated pAbs-AuNPs"

The FT-IR spectrum analysis of naive pAbs and its bioconjugated entity showed initial absorption peaks at 3,300 to 3,400 cm^{-1}, 2,604 cm^{-1}, and 1,400 to 1,300 cm^{-1} due to strong stretching vibrations of N–H, S–H, and S=O of thiol and sulphonyl groups along with convoluted O–H bands, respectively (Figure 4B). The major strong peak from 1,500 to 1,650 cm^{-1} was related to the characteristics of the protein and appeared due to the C–N and C=O stretching vibrations of peptide bonds in combination with strong N–H bending of amide I and II groups, as shown in Figure 4B. The FT-IR spectroscopy revealed a vibrational mode of the amide I region in pAbs at 1,650 cm^{-1} due to the carbonyl group –C=O stretching and amide II at 1,500 or 1,550 cm^{-1} due to N–H in-plane bending vibrations (Barth and Zscherp, 2002), since an antibody is a biological molecule protein and contains protein peptide bonds as amide bonds. The absorption spectra of these amides as amide I, II, and III and their multiband IR spectrum indicate fine components within the amides (Ji et al., 2020). In bioconjugated functionalized AuNPs, a strong peak at 3,300 to 3,400 cm^{-1} represented stretching vibrations of N–H and C–H bonds of the amide group and S–H stretching of the thiol group (Sibai et al., 1996). Compounds with the $-NH_2$ group have two IR bands between 3,400 and 3,300 cm^{-1} regardless of the molecule containing the functional group and also, some regions of the protein contain peaks from side chains or any other prosthetic or chemical group attached to the protein (Haris, 2013). In this case, rOmp28 pAbs are bioconjugated and functionalized with linked-EDC-NHS AuNPs as commonly carboxylated thiol-linked AuNPs. The absorption peaks at 1,640 cm^{-1} and 1,230 to 1,330 cm^{-1} indicated bending vibrations of N–H bonds of amide and C=O, C–N of aromatic amine, along with N–H deformation of antibody-conjugated particles. The peaks at 1,080 to 1,150 cm^{-1} were attributed to strong stretching of C–O bonds.

3.11 Slide agglutination reaction of bioconjugated AuNPs with *Brucella* WC Ag

When bioconjugated AuNPs were allowed to react with the corresponding outer membrane surface antigen of WC *Brucella abortus* S99 and *Brucella melitensis* 16M suspended in PBS at a detection range of 10^8–10^1 CFU mL^{-1}, clear visible clumps were observed at a 1:1 (50 µL each) test ratio, as shown in Figure 10. At a minimum time interval of 5 to 10 min, clumping of conjugated pAb–Ag complexes appeared on the reaction site with a lower detection limit of 10^4 CFU mL^{-1} (Figure 10). 1X PBS was used as a test control and was allowed to react with only AuNP-conjugated pAbs, where no clumping was observed, and direct strong agglutinations of the test sample was considered as "test positive" for the applied assay.

3.12 The sensitivity and specificity assays with inter- and intraspecies

On estimating the direct-differential agglutination assay with WC Ag at a concentration of 1×10^4 CFU mL^{-1} of *Brucella* standard strains and a total of 36 randomly selected human clinical isolates, strong positive agglutinations in the test results were obtained which determined the relative efficacy of the method employed, and the high sensitivity of the developed assay (see Figure 11 and Supplementary Table S1; Supplementary Table S3). Similarly, WC Ag (at an optimized test LOD) of 26 *Brucella* closely related and non-related other bacterial species reacted to agglutinate for about 5 to 10 min and for which strong negative results were obtained (Figure 12 and Supplementary Table S2). Hence, on analysis, it was found that the direct-differential slide agglutination assay is both sensitive and specific in whole-cell detection of the genus *Brucella*.

3.13 Validation of the direct-agglutination assay with spiked studies

For validation and evaluation of the direct slide agglutination assay, differential agglutination with *Brucella* WC Ag spiked clinical and non-clinical samples was performed at an optimized detection limit of 10^4 CFU mL^{-1}. The clinical samples such as cow urine, FBS, human sera, human urine and non-clinical samples such as cow milk and human milk have shown no background interference with Ag–Ab agglutination reactions on using AuNP-conjugated rOmp28 mice IgG pAbs, which explained the relatively low toxicity of conjugated constructs (see Figure 13). In fact, a clear, rapid, and strong positive agglutination reaction appeared when the assay was performed within 5 to 10 min. It was clearly inferred during the agglutination reaction that the clumping of modified nanomaterial functionalized with the IgG antibody and its complexes with spiked *Brucella* WC antigens first appeared in spiked sera samples (within 5 min), followed by milk and urine samples after 5 min. This therefore indicated that the developed rapid slide agglutination assay is quite efficient for on-field application in the screening of *Brucella* infection directly from a patient's blood. Also, this assay successfully detected all the spiked standard strains of *Brucella* used in spiking study at an optimized LOD of 10^4 CFU mL^{-1}. The validation study also suggested that the selection of conserved and specific targets for rapid WC Ag detection has relatively high potential to develop sensitive, specific, and accurate detection assays with minimum cross-reactivity and maximum test performance for the confirmation of positive clinical cases. Also, for futuristic approaches, new prospects can be focused on modification of the test antibody to monospecific monoclonal forms or bioengineered antibody fragments to enhance species level biodetection using the proposed direct-differential agglutination assay.

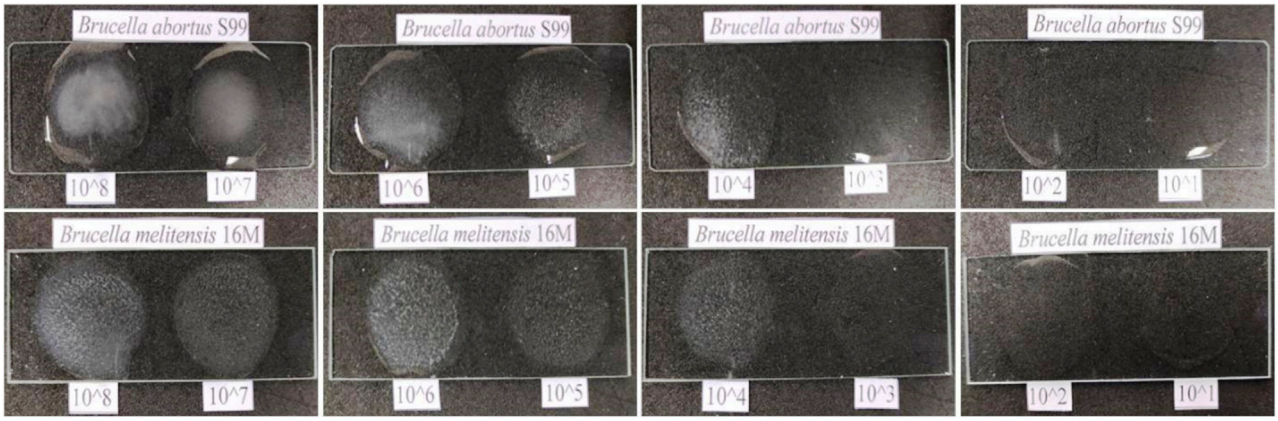

FIGURE 10
Rapid direct-differential slide agglutination assay determining a lower limit of detection (LOD) of 10^4 CFU mL^{-1} at an experimental detection range of 10^8–10^1 CFU mL^{-1} on positive agglutination reaction observed with two standard bacterial species of genus *Brucella* (*Brucella abortus* S99 and *Brucella melitensis* 16M). No hook or prozone effect was observed during positive agglutinations.

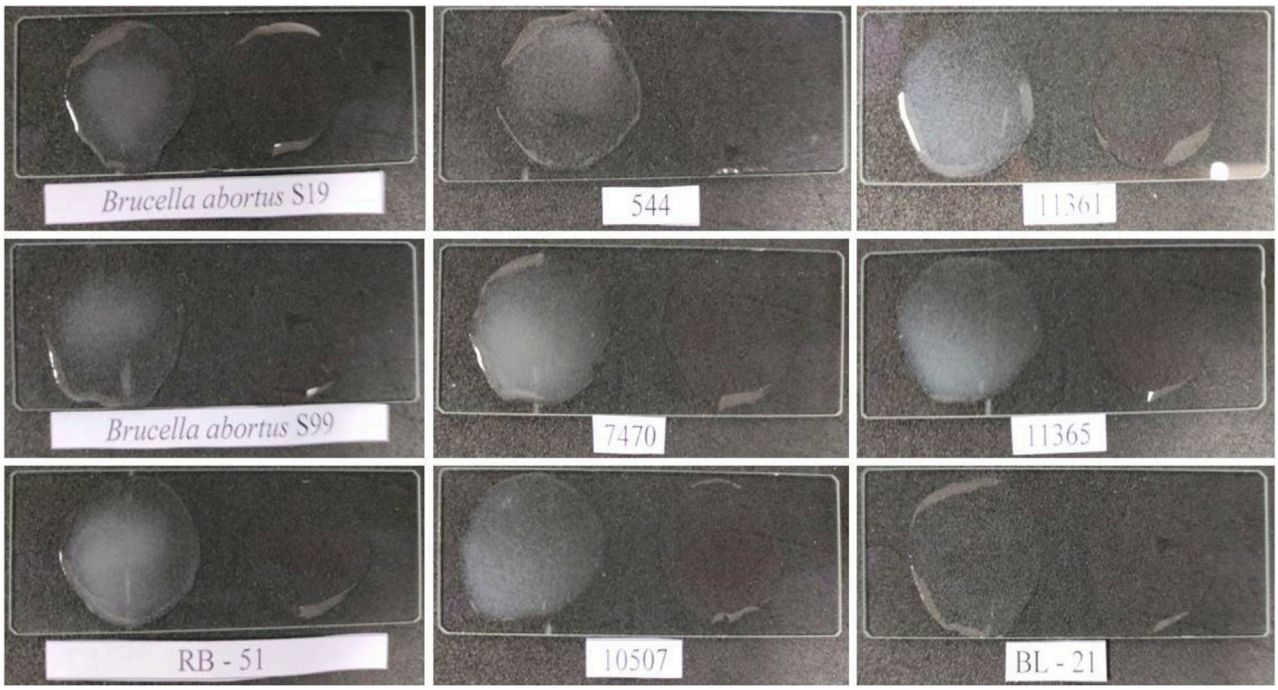

FIGURE 11
Estimation for investigation of test sensitivity of direct-differential slide agglutination assay with WC antigen of *Brucella* standard strains at an obtained experimental LOD of 10^4 CFU mL^{-1} with *Escherichia coli* (BL-21) and 1X PBS having bioconjugated AuNPs without test antigen as a negative test control ("Test Negative"). A rapid and strong agglutination reaction with all *Brucella* standard strains/biotypes was observed, and the results were inferred as "Test Positive" for the developed assay. No agglutination was observed with the test negative *Escherichia coli* and PBS.

3.14 Comparative S-ELISA for *Brucella* whole-cell detection using mice IgG pAbs

To determine the efficacy of the purified rOmp28 mice IgG detection antibody used in the agglutination assay for the evaluation of its rapid immuno-reactivity and minimum detection limits, a comparative S-ELISA for WC Ag detection of standard strains, closely related and non-related bacterial species, and human clinical isolates was performed. The S-ELISA assay detected WC CFU at a minimum LOD of 10^3 CFU mL^{-1} with a detection range of 10^2–10^8 CFU mL^{-1} (Figure 14). *Brucella* standard strains were detected at 10-fold serial dilution with linearity in the trend, a logarithmic regression equation of $y = -0.489 \ln(x) + 1.685$, and $R^2 = 0.846$, as shown in Figure 14A. Also, *Brucella* clinical isolates

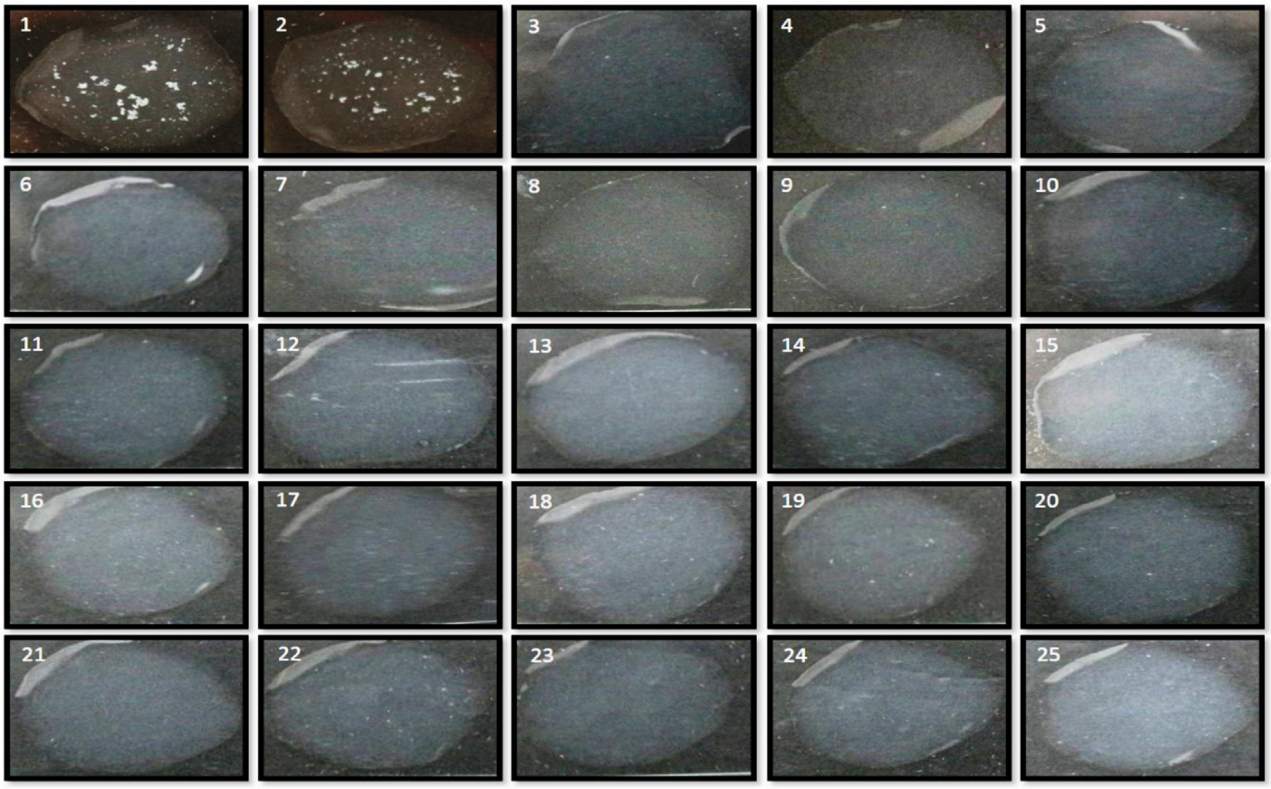

FIGURE 12
Estimation for investigation of test specificity of direct-differential slide agglutination assay with WC antigen of *Brucella* and other closely related and non-related bacterial species to evaluate the cross-reactivity at an obtained experimental LOD of 10^4 CFU mL^{-1}. No clumping for positive agglutination reaction was observed, and the results were inferred as "Test Negative" for the developed assay on testing along with positive test controls (*Brucella abortus* S99 and *Brucella melitensis* 16M) of *Brucella*.

randomly screened at 10-fold serial dilution using the rOmp28 mice IgG detection antibody (at 100 μg mL^{-1}) presented an experimental LOD of 10^3 CFU mL^{-1} (see Figure 14B). The 100% detection of *Brucella* clinical and standard species determined the relative sensitivity and potential efficacy of the optimized test antibody for the developed slide-agglutination assay. In order to determine the comparative specificity of the agglutination assay, cross-reactions with other closely related and non-related bacterial species were evaluated using the rOmp28 mice IgG detection antibody in the double-antibody S-ELISA format, and no intraspecies cross-reactivity was observed at the obtained LOD with similar comparative S-ELISA (see Figure 14C). The minimum LOD was obtained at an experimental cut-off value of 0.3 OD at 495 nm absorbance and was found to have "no detection" as compared to the < 0.5 OD value of positive S-ELISA for WC detection of *Brucella*. In comparison, S-ELISA presented an LOD of 10^3 CFU mL^{-1} with a detection range of 10^2–10^8 CFU mL^{-1} using double-antibody at optimized concentrations (WC rabbit IgG at 10 μg mL^{-1} as the capture antibody and rOmp28 mice IgG at 100 μg mL^{-1} as the detection antibody). We also utilized a labeled anti-species enzyme-conjugated secondary antibody with an experimental run-time of approximately 4 to 5 h. In comparison, although a 1 $\log_{10}$ higher LOD was obtained with the direct-differential slide agglutination assay, it offers minimum time of performance, easy to operate, rapid, cost-effectiveness, sensitive, specific, no hook or prozone effects, higher capacity for multiple sample screening, no false positive or false negative results, and requires minimum expertise or intensive labor. Therefore, recombinant rOmp28 IgG pAbs of *Brucella melitensis* 16M has a high potential for direct-differential WC detection of the genus *Brucella* and can be deployed for early clinical diagnosis.

4 Discussion

Brucella infection is severely contagious with frequent relapse due to its diverse disease pool, intracellular life, antibiotic resistance, and no available vaccines. In our present study, functionalized bioconjugated gold nanoparticles were used in direct-differential whole-cell agglutination of *Brucella* as a rapid, sensitive, and specific detection method for its potential on-field application. We observed a strong positive agglutination reaction due to the rapid Ag–Ab complexes formed with bioconjugated AuNPs, and this method involves a low risk of infection. For *Brucella* rapid detection, many assays have been reported using modified rapid slide agglutination test (RSAT) over conventional RSAT to distinguish rough and smooth strains of *Brucella* (Shell et al., 2012). Microplate agglutination testing (MAT) using multiple recombinant antigen-

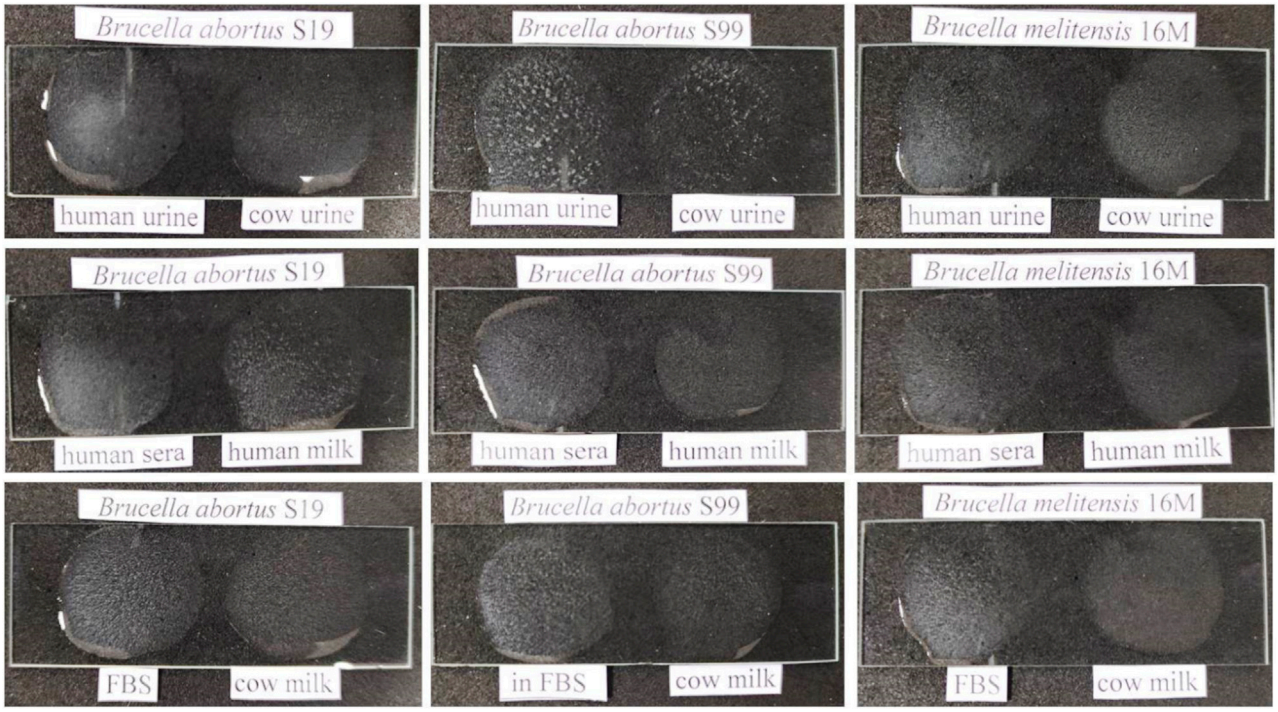

FIGURE 13
Evaluation of experimental validation for rapid and direct-differential slide agglutination assay with spiked WC Ags of *Brucella* standard strains (*Brucella abortus* S19, *Brucella abortus* S99, and *Brucella melitensis* 16M) in different clinical (cow and human urine, FBS-fetal bovine sera, and human sera) and non-clinical (cow and human milk) matrices at an obtained experimental LOD of 10^4 CFU mL^{-1}. A clear, rapid, and strong positive agglutination reaction appeared initially in spiked sera samples, followed by milk and urine samples with no relative interference of test matrices.

coated latex beads for *Brucella canis* identification and tube agglutinin testing (TAT) using antigenic solutions of safranin stained *Brucella canis* were reported (Kimura et al., 2008; Castillo et al., 2014). Latex agglutination testing (LAT) with soluble *Brucella melitensis* periplasmic proteins (SBPPs) for the detection of ovine brucellosis offered better efficacy over the buffered plate agglutination test (BPAT), RBT, SAT, and I-ELISA, but they are less specific with a high rate of false-positives (Ismael et al., 2016). A comparison between the sero-agglutination test (SAT), Coombs anti-*Brucella* test, and brucellaCapt test revealed high sensitivity with brucellaCapt, but it also lacks specificity at lower diagnostic titers (Orduna et al., 2000). Similarly, combined confirmatory tests such as complement fixation test (CFT) and agar gel precipitation test (AGPT) were used together with agglutination assays employing R-LPS antigens, but they also presented prozone effects, high cost, long turn-around time, low sample capacitance, intensive labor, and a high rate of false positives and negatives (Hollett, 2006). On the other hand, our investigation indicated that the employment of rOmp28 as a specific surface marker of *Brucella* is specific, sensitive, and accurate in the detection of whole-cell bacteria with bioconjugated AuNPs. Clinical validation of our study showed direct testing of sample matrices where the availability of *Brucella* is significantly high. Also, AuNPs have a natural tendency to conjugate with active biological moieties and their nanobio interfaces involve amine and thiol group couplings during pAb bioconjugations (Arvizo et al., 2010). We therefore explored specific antigen–antibody-based selective immuno-reaction platforms by conjugating AuNPs for sensitive bacterial detection. Our findings suggest that the drawbacks of serology-based identification can be improved using suitable bioconjugated nanoparticles for early disease detection, diagnosis, and therapeutics (Arruebo et al., 2009). In our study, we modified AuNPs by initial co-reduction for MHA SAM linking, and MHA further favored bi-functional EDC/NHS coupling to preserve the biological activity, stability, and binding affinity of the *Brucella*-specific rOmp28 antibody. The multivalent surface presentations of active functional groups by AuNPs have enhanced covalent linking and ionic adsorptions with the primary amines (N-end) and carboxylic acid ends (C-end) of the antibody for surface immobilization (Fratila et al., 2014; Jazayeri et al., 2016). Hence, conjugation with specific IgG pAbs provided targeted multivalent capture of whole-cell bacteria (Busch et al., 2019). Omp28 is a sensitive diagnostic marker, a non-LPS precursor protein, and a specific immunogen of major OMPs of group-3 immunodominant *Brucella* antigens and has evolved as a selective candidate for improved serological detection of conserved epitopes among *Brucella melitensis* and *Brucella abortus* (Liang et al., 2010; Lim et al., 2012a; Kumar et al., 2012; Ahmed et al., 2015; Manat et al., 2016; Hisham and Ashhab, 2018; He et al., 2022). Its high sensitivity, specificity, and accuracy were discovered in I-ELISA and LAT with the latter showing more rapid detection of anti-*Brucella* antibodies in human and bovine brucellosis and a high degree of suitability in rapid agglutination tests for clinical serodiagnosis (Kumar et al., 2008; Chaudhuri et al., 2010; Lim et al., 2012b; Tiwari et al., 2013; Koyuncu et al., 2018). We therefore selected rOmp28 pAbs in our

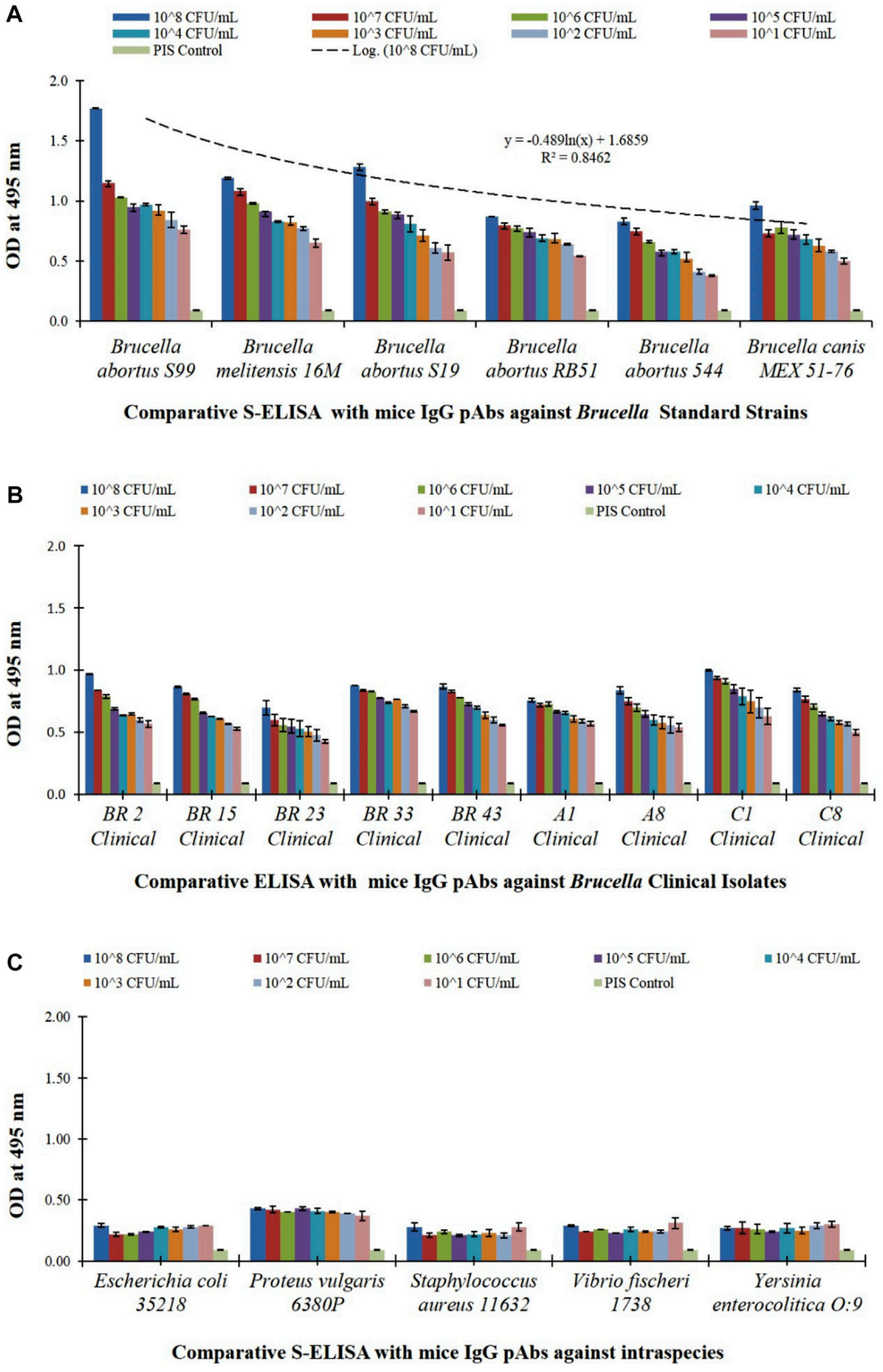

FIGURE 14
Comparative S-ELISA assay for *Brucella* intact WC detection and for evaluation of cross-reactivity with optimized bioconjugated test antibody (rOmp28 mice polyclonal IgG detection antibody) used in the direct-differential slide agglutination assay, with **(A)** S-ELISA graph plot showing WC detection of 10-fold serial diluted WC Ag of *Brucella* standard species at an LOD of 10^3 CFU mL^{-1} with a detection range of 10^2–10^8 CFU mL^{-1} along the x-axis and absorbance at 495 nm along the y-axis. An experimental logarithmic regression coefficient value of R^2 = 0.8462 was obtained with the variable model equation of y = –0.489ln(x) + 1.6859, showing linearity in the trend of *Brucella* WC Ag detection, **(B)** S-ELISA graph plot showing WC detection of 10-fold serial diluted, randomly screened WC Ag of *Brucella* human clinical isolates at an LOD of 10^3 CFU mL^{-1} with a detection range of 10^2–10^8 CFU mL^{-1} along the x-axis and absorbance at 495 nm along the y-axis, and **(C)** S-ELISA graph plot showing WC detection of 10-fold serial diluted
(*Continued*)

FIGURE 14 (Continued)
WC Ag of *Brucella* closely related bacterial intraspecies (*Escherichia coli*, *Proteus vulgaris*, *Staphylococcus aureus*, *Vibrio fischeri*, and *Yersinia enterocolitica*) for evaluation of cross-reactivity at a detection range of 10^2–10^8 CFU mL^{-1} along the x-axis and absorbance at 495 nm along the y-axis. A cut-off OD value of < 0.5 was obtained with no detection as compared to a positive S-ELISA OD value of > 0.5 for *Brucella* standard species and clinical isolates.

detection assay because *bp*26 gene sequencing for the immunogenic BP26 periplasmic protein had revealed identical sequences with minor differences in *Brucella abortus* S19 and *Brucella melitensis* 16M can be abbreviated as for *Brucella* genus like *B. suis* and *B. ovis*, and because it can potentially detect species of *Brucella* (Seco-Mediavilla et al., 2003). We observed that modification of the nanometallic moiety is important in developing a sensitive diagnostic assay. The 16-MHA long chain aliphatic linker (n-alkanethiolate chains) has modified AuNPs for an apparent increase in Ag-to-Ab ratios, increased thiol linkages with rOmp28 pAbs, reduction of non-specific binding, eliminated toxic effects, fabricated stable molecular assemblies, and high passivation of pAbs. IgG antibodies contain an F(ab) region with an amine group and an Fc region with N-glycan residues. A non-specific binding to F(ab) causes inactivation of the antibody by blocking antigen binding sites in variable regions of heavy and light chains (Welch et al., 2017). In this study, 16-MHA acted as the "master molecule" with thiol anchorage allowing fabrication of gold nanoparticles to minimize F(ab) bindings, and, together with EDC/NHS, binds to the Fc region of heavy chains by activating –COOH groups of antibodies to form reactive N-hydroxysuccinimide esters that further bind with amino peptide groups (Bhadra et al., 2015; Drozd et al., 2021). Thus, toxic reactive intermediates of carbodiimide are stabilized by these esterified sulfo-succinimides (NHS). Moreover, in this study, we have evaluated toxic effects with validation studies using clinical samples without the test analyte, and no patching, hooks, or agglomeration of samples was observed. The developed agglutination assay is highly specific and sensitive, and for further species level detection of *Brucella*, we suggest the use of the monospecific monoclonal antibody for bioconjugation. Second, the LOD of 10^4 CFU mL^{-1} for the differential assay can be minimized by using *Brucella*-specific OMPs as combined fusion proteins. Lastly, nanometallic particle integration with the antibody can be replaced with nanoscale metal organic frameworks (MOFs) for further modifications, since the infecting dose of *Brucella* is very low with 10 to 100 CFU mL^{-1} of bacteria required in early on-set of brucellosis infection (Yagupsky, 2022). Therefore, for early disease diagnosis and prevention, more advert nanotechniques with selective markers of *Brucella* are required. In this present study, we selectively used the rOmp28 surface protein marker and found an excellent rate of agglutination in positive test samples, showing no false positives or cross-reactivity with the optimized assay. Therefore, the developed agglutination assay can be used as a preliminary test method in direct whole-cell detection of *Brucella* antigens available in the common disease matrix. Moreover, this assay is rapid, easy to apply, cost-effective, and requires no laboratory set-ups for its clinical application and can be deployed for on-field testing of differential diseased cases where pathogen identification is misleading and under-diagnosed.

5 Conclusion

Brucellosis is the most contagious, debilitative, and widespread common zoonosis, with acute, sub-acute, and chronic disease presentation worldwide, since low doses of 10 to 100 CFU mL^{-1} of bacteria are capable of spreading its infection. In our present study, we therefore developed a concurrent, highly sensitive, differentially rapid, and direct agglutination-based diagnostic assay using 16-MHA SAMs linked functionalized metal oxide gold nanoparticles. This assay offered maximum detection accuracy at an LOD of 1×10^4 CFU mL^{-1} with limited test matrices, and is simple, safe, and reliable with minimum time consumption required for employment in on-field test environments. It is the first assay of its kind with direct differential detection of intact whole-cell *Brucella* achieved at an optimized detection range of 10^1–10^8 CFU mL^{-1}, with diagnostic potential of the recombinant rOmp28 surface protein marker of *Brucella melitensis* 16M. Bioconjugated AuNPs constructs with specific rOmp28 IgG pAbs showed good agreement with in-house available comparative S-ELISA and favorable clinical validation with a related and non-related battery of test pathogens. The sensitivity and specificity of the developed assay is ≥ 98 % which shows the serological potential of the rOmp28 antigen with unique epitopes for limited homology within genus *Brucella*. Moreover, this assay has detected the whole-cell *Brucella* antigen with no similar cross reactions with five closely related bacteria in the S-ELISA format at an LOD of 10^3 CFU ml^{-1}. No toxicity of the functionalized bioconjugated AuNPs was observed as no hemolysis of blood serum was found, and we obtained 100 % true positive agglutinations. The performance time of the assay is minimal, and it requires only 2 to 3 drops of valuable test samples for preliminary diagnostic examination using standard methods. It is therefore sensitive for detecting whole-cell bacteria in low disease burden and a true alternate method for early disease detection. To conclude, we have developed and evaluated the performance of a rapid and direct-differential slide agglutination assay with reduced non-specific reactivity. The comprehensive methodology for the synthesis of biologically stable gold nanoparticles is promising and can be utilized as a potential ready-to-use agglutination-based differential diagnostic method in the low-resource settings of the developing world where brucellosis is highly endemic. Furthermore, this direct agglutination assay can be used for primary characterization of bacterial isolates, and after screening with this agglutination assay, the results can be provided by efficient medical set-ups for management of early clinical cases.

Data availability statement

The original contributions presented in the study are included in the article/Supplementary Material; further inquiries can be directed to the corresponding author.

Ethics statement

The animal study was reviewed and approved by the Institutional Animal Ethics Committee (No: 37/GO/Rbi/S/99/CPCSEA and IAEC MB-43/57/DTS Dated: 14/06/2018 and IAEC BDTE-01/59/SP Dated: 05/06/2020).

Author contributions

DT and RH designed the experiments. RH performed all the experiments and manuscript writing. PY helped in maintaining bacterial cultures. MZ performed SEM, TEM, and TEM-SAED for NP characterization. DT, RP, MZ, and RH performed characteristic analysis of the gold nanomaterial. DT and RH evaluated and analyzed all the experimental results. DT accepted, reviewed, and revised the complete manuscript. This research work was completed by RH under the proper guidance of DT.

Acknowledgments

The authors are thankful to D. K. Dubey, Director, Defence Research and Development Establishment, Defence Research and Development Organisation (DRDO), Jhansi Road, Gwalior—474002 (M.P.), India, for his encouragement and continuous support of this study. Also, the authors extend their acknowledgements to faculty and technical staff of A.P.J. Abdul Kalam Central Instrumentation Facility (C.I.F.), Jiwaji University, Gwalior, Biosensor Development Division and the Electron Microscopy Division, DRDE (DRDO), Gwalior, India, for providing the necessary instrumentation for characterization. This paper has been allotted the DRDE accession no. DRDE/BDTE/50/2020.

Conflict of interest

The authors declare that the research was conducted in the absence of any commercial or financial relationships that could be construed as a potential conflict of interest.

Publisher's note

All claims expressed in this article are solely those of the authors and do not necessarily represent those of their affiliated organizations, or those of the publisher, the editors, and the reviewers. Any product that may be evaluated in this article, or claim that may be made by its manufacturer, is not guaranteed or endorsed by the publisher.

Supplementary material

The Supplementary Material for this article can be found online at: https://www.frontiersin.org/articles/10.3389/fnano.2023.1132783/full#supplementary-material

References

Ahmed, I. M., Khairani-Bejo, S., Hassan, L., Bahaman, A. R., and Omar, A. R. (2015). Serological diagnostic potential of recombinant outer membrane proteins (rOMPs) from Brucella melitensis in mouse model using indirect enzyme-linked immunosorbent assay. *BMC Vet. Res.* 11, 275. doi:10.1186/s12917-015-0587-2

Al Dahouk, S., and Nockler, K. (2011). Implications of laboratory diagnosis on brucellosis therapy. *Expert Rev. anti. Infect. Ther.* 9, 833–845. doi:10.1586/eri.11.55

Aldosari, F. M. M. (2022). Characterization of labeled gold nanoparticles for surface-enhanced Raman scattering. *Molecules* 27, 892. doi:10.3390/molecules27030892

Ansar, S. M., Chakraborty, S., and Kitchens, C. L. (2018). pH-Responsive mercaptoundecanoic acid functionalized gold nanoparticles and applications in catalysis. *Nanomater. (Basel)* 8, 339. doi:10.3390/nano8050339

Arruebo, M., Valladares, M., and Gonzalez-Fernandez, A. (2009). Antibody-conjugated nanoparticles for biomedical applications. *J. Nanomater* 2009, 1–24. doi:10.1155/2009/439389

Arvizo, R., Bhattacharya, R., and Mukherjee, P. (2010). Gold nanoparticles: Opportunities and challenges in nanomedicine. *Expert Opin. Drug Deliv.* 7, 753–763. doi:10.1517/17425241003777010

Bagheri Nejad, R., Krecek, R. C., Khalaf, O. H., Hailat, N., and Arenas-Gamboa, A. M. (2020). Brucellosis in the Middle East: Current situation and a pathway forward. *PLoS Negl. Trop. Dis.* 14, e0008071. doi:10.1371/journal.pntd.0008071

Bakri, F. G., AlQadiri, H. M., and Adwan, M. H. (2018). The highest cited papers in brucellosis: Identification using two databases and review of the papers' major findings. *Biomed. Res. Int.* 1, 1–10. doi:10.1155/2018/9291326

Baltierra-Uribe, S. L., Chanona-Perez, J. J., Mendez-Mendez, J. V., Perea-Flores, M. J., Sanchez-Chavez, A. C., Garcia-Perez, B. E., et al. (2019). Detection of *Brucella abortus* by a platform functionalized with protein A and specific antibodies IgG. *Microsc. Res. Tech.* 82, 586–595. doi:10.1002/jemt.23206

Bartczak, D., and Kanaras, A. G. (2011). Preparation of peptide-functionalized gold nanoparticles using one pot EDC/sulfo-NHS coupling. *Langmuir* 27, 10119–10123. doi:10.1021/la2022177

Barth, A., and Zscherp, C. (2002). What vibrations tell about proteins. *Q. Rev. Biophys.* 35, 369–430. doi:10.1017/s0033583502003815

Barua, A., Kumar, A., Thavaselvam, D., Mangalgi, S., Prakash, A., Tiwari, S., et al. (2016). Isolation & characterization of *Brucella melitensis* isolated from patients suspected for human brucellosis in India. *Indian J. Med. Res.* 143, 652–658. doi:10.4103/0971-5916.187115

Bhadra, P., Shajahan, M. S., Bhattacharya, E., and Chadha, A. (2015). Studies on varying n-alkanethiol chain lengths on a gold coated surface and their effect on antibody-antigen binding efficiency. *RSC Adv.* 5, 80480–80487. doi:10.1039/c5ra11725a

Biao, L., Tan, S., Meng, Q., Gao, J., Zhang, X., Liu, Z., et al. (2018). Green synthesis, characterization and application of proanthocyanidins-functionalized gold nanoparticles. *Nanomaterials* 8, 53. doi:10.3390/nano8010053

Boggiatto, P. M., Schaut, R. G., Kanipe, C., Kelly, S. M., Narasimhan, B., Jones, D. E., et al. (2019). Sustained antigen release polyanhydride-based vaccine platform for immunization against bovine brucellosis. *Heliyon* 5, e02370. doi:10.1016/j.heliyon.2019.e02370

Busch, R. T., Karim, F., Weis, J., Sun, Y., Zhao, C., and Vasquez, E. S. (2019). Optimization and structural stability of gold nanoparticle–antibody bioconjugates. *ACS Omega* 4, 15269–15279. doi:10.1021/acsomega.9b02276

Castillo, Y., Tachibana, M., Kimura, Y., Kim, S., Ichikawa, Y., Endo, Y., et al. (2014). Microplate agglutination test for canine brucellosis using recombinant antigen-coated beads. *Int. Sch. Res. Not.* 2014, 1–4. doi:10.1155/2014/348529

Centers for Disease Control and Prevention (CDC) (2005). Public health consequences of a false-positive laboratory test result for *Brucella* – Florida, Georgia, and Michigan. *MMWR Morb. Mortal. Wkly. Rep.* 57, 603–605.

Chaudhuri, P., Prasad, R., Kumar, V., and Gangaplara, A. (2010). Recombinant OMP28 antigen-based indirect ELISA for serodiagnosis of bovine brucellosis. *Mol. Cell Probes* 24, 142–145. doi:10.1016/jmcp.2009.12.002

Choktaweesak, N., Krasathong, P., and Ammaranond, P. (2016). Development of enhancing agglutination reaction using gold nanoparticle for pre-transfusion testing. *Transfus. Med.* 26, 360–364. doi:10.1111/tme.12330

Dey, A., Yogamoorthy, A., and Sundarapandian, S. M. (2018). Green synthesis of gold nanoparticles and evaluation of its cytotoxic property against colon cancer cell line. *Res. J. Life Sci. Bioinform. Pharm. Chem. Sci.* 4, 1–17. doi:10.26479/2018.0406.01

Di Bonaventura, G., Angeletti, S., Ianni, A., Petitti, T., and Gherardi, G. (2021). Microbiological laboratory diagnosis of human brucellosis: An overview. *Pathogens* 10, 1623. doi:10.3390/pathogens10121623

Drozd, M., Karon, S., and Malinowska, E. (2021). Recent advancements in receptor layer engineering for applications in SPR-based immunodiagnostics. *Sensors* 21, 3781. doi:10.3390/s21113781

El-Sayed, A., and Awad, W. (2018). Brucellosis: Evolution and expected comeback. *Int. J. Vet. Sci. Med.* 6, S31–S35. doi:10.1016/j.ijvsm.2018.01.008

Ellis, A. V., Chong, S., and Jansen, M. (2008). Formation of an α-cyclodextrin/16-mercaptohexadecanoic acid complex and its deposition on gold surfaces. *J. Incl. Phenom. Macrocycl. Chem.* 63, 267–272. doi:10.1007/s10847-008-9516-3

Etemadi, A., Moniri, R., Neubauer, H., Dasteh Goli, Y., and Alamian, S. (2019). Laboratory diagnostic procedures for human brucellosis: An overview of existing approaches. *Jundishapur J. Microbiol.* 12, e91200. doi:10.5812/jjm.91200

Fang, A., Feng, D., Luo, X., and Shi, F. (2022). Gold nanoparticles prepared with cyclodextrin applied to rapid vertical flow technology for the detection of brucellosis. *Biosens. (Basel)* 12, 531. doi:10.3390/bios12070531

Fernandez-Ponce, C., Munoz-Miranda, J. P., de Los Santos, D. M., Aguado, E., Garcia-Cozar, F., and Litran, R. (2018). Influence of size and surface capping on photoluminescence and cytotoxicity of gold nanoparticles. *J. Nanopart. Res.* 20, 305. doi:10.1007/s11051-018-4406-0

Fratila, R. M., Mitchell, S. G., del Pino, P., Grazu, V., and de la Fuente, J. M. (2014). Strategies for the biofunctionalization of gold and iron oxide nanoparticles. *Langmuir* 30, 15057–15071. doi:10.1021/la5015658

Galinska, E. M., and Zagorski, J. (2013). Brucellosis in humans-etiology, diagnostics, clinical forms. *Ann. Agric. Environ. Med.* 20, 233–238.

Gao, Y., Zhou, Y., and Chandrawati, R. (2020). Metal and metal oxide nanoparticles to enhance the performance of enzyme-linked immunosorbent assay (ELISA). *ACS Appl. Nano Mat.* 3, 1–21. doi:10.1021/acsanm.9b02003

Ghazy, N. A., Abdel Aziz, W. R., Shell, W. S., and Samy, A. A. (2016). Efficiency of different preparations of rapid slide agglutination antigens for the diagnosis of bovine and ovine brucellosis. *Asian J. Anim. Vet. Adv.* 11, 399–404. doi:10.3923/ajava.2016.399.404

Gorbachevskii, M. V., Kopitsyn, D. S., Kotelev, M. S., Ivanov, E. V., Vinokurov, V. A., and Novikov, A. A. (2018). Amplification of surface-enhanced Raman scattering by the oxidation of capping agents on gold nanoparticles. *RSC Adv.* 8, 19051–19057. doi:10.1039/C8RA00417J

Govindasamy, K., Etter, E. M. C., Harris, B. N., Rossouw, J., Abernethy, D. A., and Thompson, P. N. (2021). Knowledge of brucellosis, health-seeking behaviour, and risk factors for *Brucella* infection amongst workers on cattle farms in Gauteng, South Africa. *Pathogens* 10, 1484. doi:10.3390/pathogens10111484

Guan, P., Wu, W., and Huang, D. (2018). Trends of reported human brucellosis cases in mainland China from 2007 to 2017: An exponential smoothing time series analysis. *Environ. Health Prev. Med.* 23, 23. doi:10.1186/s12199-018-0712-5

Haider, A. J., Shabeeb, D. A., and Mohammed, A. T. (2016). Synthesis and stabilization of gold nanoparticles by inverse reduction method using sodium citrate and sodium borohydride as reducing agent. *J. Univ. Anbar Pure Sci.* 10, 37–47. doi:10.37652/juaps.2016.132440

Hans, R., Yadav, P. K., Sharma, P. K., Boopathi, M., and Thavaselvam, D. (2020). Development and validation of immunoassay for whole cell detection of *Brucella abortus* and *Brucella melitensis*. *Sci. Rep.* 10, 8543. doi:10.1038/s41598-020-65347-9

Haris, P. I. (2013). Probing protein-protein interaction in biomembranes using Fourier transform infrared spectroscopy. *Biochim. Biophys. Acta Biomembr.* 1828, 2265–2271. doi:10.1016/j.bbamem.2013.04.008

Hashemi, H., Varshosaz, J., Fazeli, H., Sharafi, S. M., Mirhendi, H., Chadeganipour, M., et al. (2019). Rapid differential diagnosis of vaginal infections using gold nanoparticles coated with specific antibodies. *Med. Microbiol. Immunol.* 208, 773–780. doi:10.1007/s00430-019-00622-9

He, C. Y., Yang, J. H., Ye, Y. B., Zhao, H. L., Liu, M. Z., Yang, Q. L., et al. (2022). Proteomic and antibody profiles reveal antigenic composition and signatures of bacterial ghost vaccine of brucella abortus A19. *Front. Immunol.* 13, 874871. doi:10.3389/fimmu.2022.874871

Hinterwirth, H., Kappel, S., Waitz, T., Prohaska, T., Lindner, W., and Lammerhofer, M. (2013). Quantifying thiol ligand density of self-assembled monolayers on gold nanoparticles by inductively coupled plasma-mass spectrometry. *ACS Nano* 7, 1129–1136. doi:10.1021/nn306024a

Hisham, Y., and Ashhab, Y. (2018). Identification of cross-protective potential antigens against pathogenic brucella spp. through combining pan-genome analysis with reverse vaccinology. *J. Immunol. Res.* 2018, 1–15. doi:10.1155/2018/1474517

Hollett, R. B. (2006). Canine brucellosis: Outbreaks and compliance. *Theriogenology* 66, 575–587. doi:10.1016/j.theriogenology.2006.04.011

Holt, H. R., Bedi, J. S., Kaur, P., Mangtani, P., Sharma, N. S., Gill, J. P. S., et al. (2021). Epidemiology of brucellosis in cattle and dairy farmers of rural Ludhiana, Punjab. *Plos Negl. Trop. Dis.* 15, e0009102. doi:10.1371/journal.pntd.0009102

Ismael, A. B., Swelum, A. A., Mostafa, S. A., and Alhumiany, A. R. (2016). Latex agglutination using the periplasmic proteins antigen of *Brucella melitensis* is a successful, rapid, and specific serodiagnostic test for ovine brucellosis. *Int. J. Immunopathol. Pharmacol.* 29, 480–487. doi:10.1177/0394632016648709

Jansen, W., Demars, A., Nicaise, C., Godfroid, J., de Bolle, X., Reboul, A., et al. (2020). Shedding of Brucella melitensis happens through milk macrophages in the murine model of infection. *Sci. Rep.* 10, 9421. doi:10.1038/s41598-020-65760-0

Jazayeri, M. H., Amani, H., Pourfatollah, A. A., Pazoki-Toroudi, H., and Sedighimoghaddam, B. (2016). Various methods of gold nanoparticles (GNPs) conjugation to antibodies. *Sens. Biosensing Res.* 9, 17–22. doi:10.1016/j.sbsr.2016.04.002

Ji, Y., Yang, X., Ji, Z., Zhu, L., Ma, N., Chen, D., et al. (2020). DFT-calculated IR spectrum amide I, II and III band contributions of N-Methylacetamide fine components. *ACS Omega* 5, 8572–8578. doi:10.1021/acsomega.9b04421

Jurkin, T., Gulis, M., Drazic, G., and Gotic, M. (2016). Synthesis of gold nanoparticles under highly oxidizing conditions. *Gold Bull.* 49, 21–33. doi:10.1007/s13404-016-0179-3

Karimi, S., Moshaii, A., and Nikkhah, M. (2019). Controlled synthesis of colloidal monodisperse gold nanoparticles in a wide range of sizes: Investigating the effect of reducing agent. *Mat. Res. Express.* 6, 1150f2. doi:10.1088/2053-1591/ab3e13

Khan, A. U., Melzer, F., Hendam, A., Sayour, A. E., Khan, I., Elschner, M. C., et al. (2020). Seroprevalence and molecular identification of *Brucella* spp. in bovines in Pakistan-investigating association with risk factors using machine learning. *Front. Vet. Sci.* 7, 594498. doi:10.3389/fvets.2020.594498

Khan, M. Z., and Zahoor, M. (2018). An overview of brucellosis in cattle and humans, and its serological and molecular diagnosis in control strategies. *Trop. Med. Infect. Dis.* 3, 65. doi:10.3390/tropicalmed3020065

Khashayar, P., Amoabediny, G., Larijani, B., Hosseini, M., and Vanfleteren, J. (2017). Fabrication and verification of conjugated AuNP-antibody nanoprobe for sensitivity improvement in electrochemical biosensors. *Sci. Rep.* 7, 16070. doi:10.1038/s41598-017-12677-w

Khatoon, N., Yasin, H. M., Younus, M., Ahmed, W., Rehman, N. U., Zakaullah, M., et al. (2018). Synthesis and spectroscopic characterization of gold nanoparticles via plasma-liquid interaction technique. *AIP Adv.* 8, 015130. doi:10.1063/1.5004470

Kimura, M., Imaoka, K., Suzuki, M., Kamiyama, T., and Yamada, A. (2008). Evaluation of a microplate agglutination test (MAT) for serological diagnosis of canine brucellosis. *J. Vet. Med. Sci.* 70, 707–709. doi:10.1292/jvms.70.707

Koyuncu, I., Kocyigit, A., Ozer, A., Selek, S., Kirmit, A., and Karsen, H. (2018). Diagnostic potential of Brucella melitensis Rev1 native Omp28 precursor in human brucellosis. *Cent. Eur. J. Immunol.* 43, 81–89. doi:10.5114/ceji.2018.74877

Kumar, A., Tiwari, S., Thavaselvam, D., Sathyaseelan, K., Prakash, A., Barua, A., et al. (2012). Optimization and efficient purification of recombinant Omp28 protein of Brucella melitensis using Triton X-100 and β-mercaptoethanol. *Protein Expr. Purif.* 83, 226–232. doi:10.1016/j.pep.2012.04.002

Kumar, S., Tuteja, U., Kumar, A., and Batra, H. V. (2008). Expression and purification of the 26 kDa periplasmic protein of Brucella abortus: A reagent for the diagnosis of bovine brucellosis. *Biotechnol. Appl. Biochem.* 49, 213–218. doi:10.1042/BA20070111

Laaksonen, T., Ahonen, P., Johans, C., and Kontturi, K. (2006). Stability and electrostatics of mercaptoundecanoic acid-capped gold nanoparticles with varying counterion size. *Chemphyschem* 7, 2143–2149. doi:10.1002/cphc.200600307

Laemmli, U. K. (1970). Cleavage of structural proteins during the assembly of the head of bacteriophage T4. *Nature* 227, 680–685. doi:10.1038/227680a0

Lalsiamthara, J., and Lee, J. H. (2017). Development and trial of vaccines against *Brucella*. *J. Vet. Sci.* 18, 281–290. doi:10.4142/jvs.2017.18.S1.281

Lemos, T. S., Cequinel, J. C., Costa, T. P., Navarro, A. B., Sprada, A., Shibata, F. K., et al. (2018). Outbreak of human brucellosis in Southern Brazil and historical review of data from 2009 to 2018. *PLoS Negl. Trop. Dis.* 12, e0006770. doi:10.1371/journal.pntd.0006770

Li, L., Yin, D., Xu, K., Liu, Y., Song, D., Wang, J., et al. (2017). A sandwich immunoassay for brucellosis diagnosis based on immune magnetic beads and quantum dots. *J. Pharm. Biomed. Anal.* 141, 79–86. doi:10.1016/j.jpba.2017.03.002

Li, R., Gu, X., Liang, X., Hou, S., and Hu, D. (2019). Aggregation of gold nanoparticles caused in two different ways involved in 4-mercaptophenylboronic acid and hydrogen peroxide. *Mater. (Basel)* 12, 1802. doi:10.3390/ma12111802

Liang, L., Leng, D., Burk, C., Nakajima-Sasaki, R., Kayala, M. A., Atluri, V. L., et al. (2010). Large scale immune profiling of infected humans and goats reveals differential

recognition of Brucella melitensis antigens. *PloS Negl. Trop. Dis.* 4, e673. doi:10.1371/journal.pntd.0000673

Lim, J. J., Kim, D. H., Lee, J. J., Kim, D. G., Min, W., Lee, H. J., et al. (2012). Evaluation of recombinant 28 kDa outer membrane protein of *Brucella abortus* for the clinical diagnosis of bovine brucellosis in Korea. *J. Vet. Med. Sci.* 74, 687–691. doi:10.1292/jvms.11-0512

Lim, J. J., Kim, D. H., Lee, J. J., Kim, D. G., Min, W., Lee, H. J., et al. (2012). Protective effects of recombinant Brucella abortus Omp28 against infection with a virulent strain of Brucella abortus 544 in mice. *J. Vet. Sci.* 13, 287–292. doi:10.4142/jvs.2012.13.3.287

Lin, X., O'Reilly Beringhs, A., and Lu, X. (2021). Applications of nanoparticle-antibody conjugates in immunoassays and tumor imaging. *AAPS J.* 23, 43. doi:10.1208/s12248-021-00561-5

Lowry, O. H., Rosebrough, N. J., Farr, A. L., and Randall, R. J. (1951). Protein measurement with the folin phenol reagent. *J. Biol. Chem.* 193, 265–275. doi:10.1016/S0021-9258(19)52451-6

Lukambagire, A. S., Mendes, A. J., Bodenham, R. F., McGiven, J. A., Mkenda, N. A., Mathew, C., et al. (2021). Performance characteristics and costs of serological tests for brucellosis in a pastoralist community of Northern Tanzania. *Sci. Rep.* 11, 5480. doi:10.1038/s41598-021-82906-w

Madzharova, F., Heiner, Z., and Kneipp, J. (2020). Surface-enhanced hyper Raman spectra of aromatic thiols on gold and silver nanoparticles. *J. Phys. Chem. C Nanomater Interfaces* 124, 6233–6241. doi:10.1021/acs/jpcc.0c00294

Makula, P., Pacia, M., and Macyk, W. (2018). How to correctly determine the band gap energy of modified semiconductor photocatalysts based on UV–vis spectra. *J. Phys. Chem. Lett.* 9, 6814–6817. doi:10.1021/acs.jpclett.8b02892

Malaspina, D. C., Longo, G., and Szleifer, I. (2017). Behavior of ligand binding assays with crowded surfaces: Molecular model of antigen capture by antibody-conjugated nanoparticles. *PLoS One* 12, e0185518. doi:10.1371/journal.pone.0185518

Manat, Y., Shustov, A. V., Evtehova, E., and Eskendirova, S. Z. (2016). Expression, purification and immunochemical characterization of recombinant OMP28 protein of <i>Brucella</i> species. *Open Vet. J.* 6, 71–77. doi:10.4314/ovj.v6i2.1

Memish, Z. A., Almuneef, M., Mah, M. W., Qassem, L. A., and Osoba, A. O. (2002). Comparison of *Brucella* standard agglutination test with the ELISA IgG and IgM in patients with *Brucella* bacteremia. *Diagn. Microbiol. Infect. Dis.* 44, 129–132. doi:10.1016/s0732-8893(02)00426-1

Moreno, E., Blasco, J. M., and Moriyon, I. (2022). Facing the human and animal brucellosis conundrums: The forgotten lessons. *Microorganisms* 10, 942. doi:10.3390/microorganisms10050942

Muddapur, U. M., Alshehri, S., Ghoneim, M. M., Mahnashi, M. H., Alshahrani, M. A., Khan, A. A., et al. (2022). Plant-based synthesis of gold nanoparticles and theranostic applications: A review. *Molecules* 27, 1391. doi:10.3390/molecules27041391

MusallamII, Abo-Shehada, M. N., Hegazy, Y. M., Holt, H. R., and Guitian, F. J. (2016). Systematic review of brucellosis in the Middle East: Disease frequency in ruminants and humans and risk factors for human infection. *Epidemiol. Infect.* 144, 671–685. doi:10.1017/S0950268815002575

Ngo Thanh, V. K., Nguyen, G. D., Huynh, T. P., and Lam, Q. V. (2016). A low cost technique for synthesis of gold nanoparticles using microwave heating and its application in signal amplification for detecting *Escherichia coli* O157:H7 bacteria. *Adv. Nat. Sci. Nanosci. Nanotechnol.* 7, 035016. doi:10.1088/2043-6262/7/3/035016

Okyem, S., Awotunde, O., Ogunlusi, T., Riley, M. B., and Driskell, J. D. (2021). High-affinity points of interaction on antibody allow synthesis of stable and highly functional antibody-gold nanoparticle conjugates. *Bioconjug Chem.* 32, 1753–1762. doi:10.1021/acs.bioconjchem.1c00261

Olsen, S. C., Boggiatto, P., White, D. M., and McNunn, T. (2018). Biosafety concerns related to *Brucella* and its potential use as a bioweapon. *Appl. Biosaf.* 23, 77–90. doi:10.1177/1535676018771983

Olsen, S. C., and Tatum, F. M. (2016). Swine brucellosis: Current perspectives. *Vet. Med.* 8, 1–12. doi:10.2147/VMRR.S91360

Orduna, A., Almaraz, A., Prado, A., Gutierrez, M. P., Garcia-Pascual, A., Duenas, A., et al. (2000). Evaluation of an immunocapture-agglutination test (Brucellacapt) for serodiagnosis of human brucellosis. *J. Clin. Microbiol.* 38, 4000–4005. doi:10.1128/JCM.38.11.4000-4005.2000

Ozdemir, M., Feyzioglu, B., Kurtoglu, M. G., Dogan, M., Dagi, H. T., Yuksekkaya, S., et al. (2011). A comparison of immuncapture agglutination and ELISA methods in serological diagnosis of brucellosis. *Int. J. Med. Sci.* 8, 428–432. doi:10.7150/ijms.8.428

Pal, D., Boby, N., Kumar, S., Kaur, G., Ali, S. A., Reboud, J., et al. (2017). Visual detection of *Brucella* in bovine biological samples using DNA-activated gold nanoparticles. *PLoS ONE* 12, e0180919. doi:10.1371/journal.pone.0180919

Pappas, G., Panagopoulou, P., Christou, L., and Akritidis, N. (2006). Biological weapons. *Cell Mol. Life Sci.* 63, 2229–2236. doi:10.1007/s00018-006-6311-4

Pengo, P., Sologan, M., Pasquato, L., Guida, F., Pacor, S., Tossi, A., et al. (2017). Gold nanoparticles with patterned surface monolayers for nanomedicine: Current perspectives. *Eur. Biophys. J.* 46, 749–771. doi:10.1007/s00249-017-1250-6

Piella, J., Bastus Neus, G., and Puntes, V. (2016). Size-controlled synthesis of sub-10-nanometer citrate-stabilized gold nanoparticles and related optical properties. *Chem. Mater* 28, 1066–1075. doi:10.1021/acs.chemmater.5b04406

Piella, J., Bastus, N. G., and Puntes, V. (2017). Size-dependent protein-nanoparticle interactions in citrate-stabilized gold nanoparticles: The emergence of the protein corona. *Bioconjug Chem.* 28, 88–97. doi:10.1021/acs.bioconjchem.6b00575

Prakash, C., Kumar, B., Singh, R. P., Singh, P., Shrinet, G., Das, A., et al. (2021). Development and evaluation of a gold nanoparticle based lateral flow assay (LFA) strip test for detection of *Brucella* spp. *J. Microbiol. Methods* 184, 106185. doi:10.1016/j.mimet.2021.106185

Pramanik, A., Gao, Y., Patibandla, S., Mitra, D., McCandless, M. G., Fassero, L. A., et al. (2021). The rapid diagnosis and effective inhibition of coronavirus using spike antibody attached gold nanoparticles. *Nanoscale Adv.* 3, 1588–1596. doi:10.1039/d0na01007c

Purwar, S., Metgud, S. C., Mutnal, M. B., Nagamoti, M. B., and Patil, C. S. (2016). Utility of serological tests in the era of molecular testing for diagnosis of human brucellosis in endemic area with limited resources. *J. Clin. Diagn. Res.* 10, DC26–DC29. doi:10.7860/JCDR/2016/15525.7311

Roddu, A. K., Wahab, A. W., Ahmad, A., Taba, P., and Sutapa, I. W. (2020). Theoretical analysis properties of gold nanoparticles resulted by bioreduction process. *J. Phys. Conf. Ser.* 1463, 012008. doi:10.1088/1742-6596/1463/1/012008

Rubach, M. P., Halliday, J. E., Cleaveland, S., and Crump, J. A. (2013). Brucellosis in low-income and middle-income countries. *Curr. Opin. Infect. Dis.* 26, 404–412. doi:10.1097/QCO.0b013e3283638104

Sagi, M., Nesher, L., and Yagupsky, P. (2017). The Bactec FX blood culture system detects *Brucella melitensis* bacteremia in adult patients within the routine 1-week incubation period. *J. Clin. Microbiol.* 55, 942–946. doi:10.1128/JCM.02320-16

Santos, R. L., Souza, T. D., Mol, J. P. S., Eckstein, C., and Paixao, T. A. (2021). Canine brucellosis: An update. *Front. Vet. Sci.* 8, 594291. doi:10.3389/fvets.2021.594291

Saxena, H. M. (2012). *inventor*. Department of Biotechnology Guru Angad Dev Veterinary and Animal Sciences University Ludhiana. (IN), assignee. US patent 20120244552A1. September 27.

Saxena, H. M., and Kaur, P. (2013). A new superagglutination test to minimize false negative and false positive results common with plate/slide agglutination tests for the diagnosis of infectious diseases. *Int. J. Trop. Dis. Health* 3, 199–209. doi:10.9734/IJTDH/2013/3405

Sayer, K. (2016). Brucellosis in fact and fiction: The story of a zoonosis. *Vet. Hist.* 18, 165–183.

Seco-Mediavilla, P., Verger, J. M., Grayon, M., Cloeckaert, A., Marin, C. M., Zygmunt, M. S., et al. (2003). Epitope mapping of the Brucella melitensis BP26 immunogenic protein: Usefulness for diagnosis of sheep brucellosis. *Clin. Diagn Lab. Immunol.* 10, 647–651. doi:10.1128/cdli.10.4.647-651.2003

Shams, A., Rahimian Zarif, B., Salouti, M., Shapouri, R., and Mirzaii, S. (2019). Designing an immunosensor for detection of *Brucella abortus* based on coloured silica nanoparticles. *Artif. Cells. Nanomed Biotechnol.* 47, 2562–2568. doi:10.1080/21691401.2019.1626403

Shell, W. S., Saad, M. A., Abd El-Razik, K. A., Sayed, M. L., and Shaapan, R. M. (2012). *Brucella ovis* as a common antigen for rapid diagnosis of rough brucellosis in cattle and sheep. *Res. J. Microbiol.* 7, 68–74. doi:10.3923/jm.2012.68.74

Shi, J. F., Gong, Q. L., Zhao, B., Ma, B. Y., Chen, Z. Y., Yang, Y., et al. (2021). Seroprevalence of brucellosis in buffalo worldwide and associated risk factors: A systematic review and meta-analysis. *Front. Vet. Sci.* 8, 649252. doi:10.3389/fvets.2021.649252

Shikha, S., Thakur, G. K., and Bhattacharyya, M. S. (2017). Facile fabrication of lipase to amine functionalized gold nanoparticles to enhance stability and activity. *RSC Adv.* 7, 42845–42855. doi:10.1039/C7RA06075K

Sibai, A., Elamri, K., Barbier, D., Jaffrezic-Renault, N., and Souteyrand, E. (1996). Analysis of the polymer-antibody-antigen interaction in a capacitive immunosensor by FTIR difference spectroscopy. *Sens. Actuators B Chem.* 31, 125–130. doi:10.1016/0925-4005(96)80028-1

Song, D., Qu, X., Liu, Y., Li, L., Yin, D., Li, J., et al. (2017). A rapid detection method of *Brucella* with quantum dots and magnetic beads conjugated with different polyclonal antibodies. *Nanoscale Res. Lett.* 12, 179. doi:10.1186/s11671-017-1941-z

Sotnikov, D. V., Barshevskaya, L. V., Zherdev, A. V., Eskendirova, S. Z., Mukanov, K. K., Mukantayev, K. K., et al. (2020). Immunochromatographic system for serodiagnostics of cattle brucellosis using gold nanoparticles and signal amplification with quantum dots. *Appl. Sci.* 10, 738. doi:10.3390/app10030738

Suchomel, P., Kvitek, L., Prucek, R., Panacek, A., Halder, A., Vajda, S., et al. (2018). Simple size-controlled synthesis of Au nanoparticles and their size-dependent catalytic activity. *Sci. Rep.* 8, 4589. doi:10.1038/s41598-018-22976-5

Suo, B., He, J., Wu, C., and Wang, D. (2021). Comparison of different laboratory methods for clinical detection of *Brucella* infection. *Bull. Exp. Biol. Med.* 172, 223–227. doi:10.1007/s10517-021-05367-1

Taheri, H., Amini, B., Kamali, M., Asadi, M., and Naderlou, E. (2020). Functionalization of anti-*Brucella* antibody based on SNP and MNP nanoparticles

for visual and spectrophotometric detection of *Brucella*. *Spectrochim. Acta A Mol. Biomol. Spectrosc.* 229, 117891. doi:10.1016/j.saa.2019.117891

Techane, S., Baer, D. R., and Castner, D. G. (2011). Simulation and modeling of self-assembled monolayers of carboxylic acid thiols on flat and nanoparticle gold surfaces. *Anal. Chem.* 83 (17), 6704–6712. doi:10.1021/ac201175a

Thavaselvam, D., Kumar, A., Tiwari, S., Mishra, M., and Prakash, A. (2010). Cloning and expression of the immunoreactive *Brucella melitensis* 28kDa outer-membrane protein (Omp28) encoding gene and evaluation of the potential of Omp28 for clinical diagnosis of brucellosis. *J. Med. Microbiol.* 59, 421–428. doi:10.1099/jmm.0.017566-0

Tiwari, S., Kumar, A., Thavaselvam, D., Mangalgi, S., Rathod, V., Prakash, A., et al. (2013). Development and comparative evaluation of a plate enzyme-linked immunosorbent assay based on recombinant outer membrane antigens Omp28 and Omp31 for diagnosis of human brucellosis. *Clin. Vaccine Immunol.* 20, 1217–1222. doi:10.1128/CVI.00111-13

Totaro, K. A., Liao, X., Bhattacharya, K., Finneman, J. I., Sperry, J. B., Massa, M. A., et al. (2016). Systematic investigation of EDC/sNHS-mediated bioconjugation reactions for carboxylated peptide substrates. *Bioconjug Chem.* 27, 994–1004. doi:10.1021/acs.bioconjchem.6b00043

Tripathi, K., and Driskell, J. D. (2018). Quantifying bound and active antibodies conjugated to gold nanoparticles: A comprehensive and robust approach to evaluate immobilization chemistry. *ACS Omega* 3, 8253–8259. doi:10.1021/acsomega.8b00591

Turkevich, J., Stevenson, P. C., and Hillier, J. (1951). A study of the nucleation and growth processes in the synthesis of colloidal gold. *Discuss. Faraday Soc.* 11, 55–75. doi:10.1039/DF9511100055

Ukita, M., Hoze, N., Nemoto, T., Cauchemez, S., Asakura, S., Makingi, G., et al. (2021). Quantitative evaluation of the infection dynamics of bovine brucellosis in Tanzania. *Prev. Vet. Med.* 194, 105425. doi:10.1016/j.prevetmed.2021.105425

Watarai, M., Kim, S., Yamamoto, J., Miyahara, K., Kazama, M., Matsuoka, S., et al. (2007). A rapid agglutination assay for canine brucellosis using antigen coated beads. *J. Vet. Med. Sci.* 69, 477–480. doi:10.1292/jvms.69.477

Wei, H., Leng, W., Song, J., Liu, C., Willner, M. R., Huang, Q., et al. (2019). Real-time monitoring of ligand exchange kinetics on gold nanoparticle surfaces enabled by hot spot-normalized surface-enhanced Raman scattering. *Environ. Sci. Technol.* 53, 575–585. doi:10.1021/acs.est.8b03144

Welch, N. G., Scoble, J. A., Muir, B. W., and Pigram, P. J. (2017). Orientation and characterization of immobilized antibodies for improved immunoassays (Review). *Biointerphases* 12, 02D301. doi:10.1116/1.4978435

Willey, T. M., Vance, A. L., van Buuren, T., Bostedt, C., Nelson, A. J., Terminello, L. J., et al. (2004). Chemically transformable configurations of mercaptohexadecanoic acid self-assembled monolayers adsorbed on Au(111). *Langmuir* 20, 2746–2752. doi:10.1021/la036073o

Wu, H., Zuo, Y., Cui, C., Yang, W., Ma, H., and Wang, X. (2013). Rapid quantitative detection of *Brucella melitensis* by a label-free impedance immunosensor based on a gold nanoparticle-modified screen-printed carbon electrode. *Sensors (Basel)* 13, 8551–8563. doi:10.3390/s130708551

Wyatt, H. V. (2013). Lessons from the history of brucellosis. *Rev. Sci. Tech.* 32, 17–25. doi:10.20506/rst.32.1.2181

Xu, N., Wang, W., Chen, F., Li, W., and Wang, G. (2020). ELISA is superior to bacterial culture and agglutination test in the diagnosis of brucellosis in an endemic area in China. *BMC Infect. Dis.* 20, 11. doi:10.1186/s12879-019-4729-1

Yagupsky, P., Morata, P., and Colmenero, J. D. (2019). Laboratory diagnosis of human brucellosis. *Clin. Microbiol. Rev.* 33, 000733–e119. doi:10.1128/CMR.00073-19

Yagupsky, P. (2022). Preventing laboratory-acquired brucellosis in the era of MALDI-TOF technology and molecular tests: A narrative review. *Zoonotic Dis.* 2, 172–182. doi:10.3390/zoonoticdis2040016

Yohannes, M., Gill, J. P. S., Ghatak, S., Singh, D. K., and Tolosa, T. (2012). Comparative evaluation of the rose bengal plate test, standard tube agglutination test and complement fixation test for the diagnosis of human brucellosis. *Rev. Sci. Tech.* 31, 979–984. doi:10.20506/rst.31.3.2175

Zaman, M. B., Mir, R. A., and Poolla, R. (2019). Growth and properties of solvothermally derived highly crystalline Cu2ZnSnS4 nanoparticles for photocatalytic and electrocatalytic applications. *Int. J. Hydrogen Energy* 44, 23023–23033. doi:10.1016/j.ijhydene.2019.07.026

Zhang, Y., Bao, H., Miao, F., Peng, Y., Shen, Y., Gu, W., et al. (2015). Production and application of polyclonal and monoclonal antibodies against Spiroplasma eriocheiris. *Spiroplasma eriocheiris Sci. Rep.* 5, 17871. doi:10.1038/srep17871

Zhao, X., Hilliard, L. R., Mechery, S. J., Wang, Y., Bagwe, R. P., Jin, S., et al. (2004). A rapid bioassay for single bacterial cell quantitation using bioconjugated nanoparticles. *Proc. Natl. Acad. Sci. U. S. A.* 101, 15027–15032. doi:10.1073/pnas.0404806101

Zhu, L., He, J., Cao, X., Huang, K., Luo, Y., and Xu, W. (2016). Development of a double-antibody sandwich ELISA for rapid detection of *Bacillus cereus* in food. *Sci. Rep.* 6, 16092. doi:10.1038/srep16092

Zuber, A., Purdey, M., Schartner, E., Forbes, C., van der Hoek, B., Giles, D., et al. (2015). Detection of gold nanoparticles with different sizes using absorption and fluorescence based method. *Sens. Actuators B Chem.* 227, 117–127. doi:10.1016/j.snb.2015.12.044